AGU PUBLICATIONS

JGR

Journal of Geophysical Research: Atmospheres

RESEARCH ARTICLE
10.1002/2017JD027388

Key Points:
- Synthetic simulations of satellite multispectral and multiangular polarimetric measurements simultaneous with BRDF and BPDF models
- The degrees of freedom for signal can be increased by at least 2 with the addition of NIR polarimetric measurements for aerosol retrieval
- One to three additional microphysical parameters could be further retrieved with significantly decreased uncertainties by adding NIR measurements

Correspondence to:
Z. Li,
lizq@radi.ac.cn

Citation:
Hou, W., Li, Z., Wang, J., Xu, X., Goloub, P., & Qie, L. (2018). Improving remote sensing of aerosol microphysical properties by near-infrared polarimetric measurements over vegetated land: Information content analysis. *Journal of Geophysical Research: Atmospheres*, *123*, 2215–2243. https://doi.org/10.1002/2017JD027388

Received 6 JUL 2017
Accepted 31 JAN 2018
Accepted article online 13 FEB 2018
Published online 20 FEB 2018

Improving Remote Sensing of Aerosol Microphysical Properties by Near-Infrared Polarimetric Measurements Over Vegetated Land: Information Content Analysis

Weizhen Hou[1], Zhengqiang Li[1], Jun Wang[2], Xiaoguang Xu[2], Philippe Goloub[3], and Lili Qie[1]

[1]State Environment Protection Key Laboratory of Satellite Remote Sensing, Institute of Remote Sensing and Digital Earth, Chinese Academy of Sciences, Beijing, China, [2]Department of Chemical and Biochemical Engineering, Center of Global and Regional Environmental Studies, and Informatics Initiative, University of Iowa, Iowa City, IA, USA, [3]Laboratoire d'Optique Atmosphérique, Villeneuve d'Ascq, France

Abstract While polarimetric measurements contain valuable information regarding aerosol microphysical properties, polarization data in the near-infrared (NIR) bands have not been widely utilized. This paper evaluates whether the aerosol property information contents from single-viewing satellite polarimetric measurements at 1,610 and 2,250 nm can be used to improve the retrieval of aerosol parameters over vegetated land, in combination with shorter-wavelength bands (490, 670, and 870 nm). The a priori information and errors for the analysis are derived by assuming that the surface reflectance at visible wavelengths can be derived from the top of atmosphere at 2,250 nm. The information content in the synthetic data set is investigated for 10 aerosol parameters characterizing the columnar aerosol volumes (V_0^f and V_0^c), particle size distributions (r_{eff}^f, v_{eff}^f, r_{eff}^c, and v_{eff}^c), and refractive indices (m_r^f, m_i^f, m_r^c, and m_i^c) for the fine- and coarse-mode aerosol models, respectively, and one parameter C characterizing the surface polarization. The results indicate that the degrees of freedom for signal can be increased by at least 2 with the addition of NIR measurements and that one to three additional parameters could be further retrieved with significantly decreased uncertainties. In addition, the 1,610 nm band is necessary for the simultaneous retrieval of V_0^f, m_r^f, and r_{eff}^f for the fine mode dominated aerosols, while the 1,610 and 2,250 nm bands are both indispensable for retrieving V_0^f, V_0^c, m_r^c, r_{eff}^f, and r_{eff}^c in tandem for the coarse mode dominated aerosols. The analysis also reveals that C could be further retrieved by including scalar radiance and that measurement errors have significantly larger influences on the retrieval uncertainties than model errors.

1. Introduction

Atmospheric aerosols are composed of liquid and solid particles suspended in the air that originate from either natural or manmade sources (Zubko et al., 2007). By scattering and absorbing solar radiation and changing cloud microphysical properties, aerosols play an important role in both the earth-atmosphere radiation balance and the climate, and they further affect human health and visibility. Global measurements are needed to obtain various aerosol properties, including the aerosol optical depth (AOD), particle size, and refractive index (Hasekamp & Landgraf, 2005b), in order to improve the understanding of the effect of aerosols. Aerosol properties can be detected via remote sensing from ground-based, airborne, and satellite platforms (Dubovik et al., 2000, 2014; Holben et al., 1998, 2001; Li et al., 2016, 2018; Ma et al., 2016; Wang, Christopher, Brechtel, et al., 2003; Wang, Christopher, Reid, et al., 2003; Wang et al., 2010). Many aerosol retrieval algorithms have been developed and improved for satellite remote sensing platforms using multispectral sensor measurements over the oceans and land (Kaufman et al., 2002; King et al., 1999; Kokhanovsky et al., 2007). The retrieval of aerosols is usually more complicated over land than over the oceans, because the contribution from the land surface reflectivity to the radiance (or reflectance) at the top of the atmosphere (TOA) is much larger; moreover, the land surface has relatively complex and variable reflectance properties (Litvinov et al., 2011).

This paper presents a theoretical study that aspires to suggest a potential improvement on existing aerosol remote sensing approaches by incorporating near-infrared (NIR) polarimetric measurements. Many previous

studies have shown that polarimetric measurements contain abundant information regarding aerosol microphysical properties (Mishchenko et al., 2007; Xu & Wang, 2015); however, most of those studies employed polarization measurements either in the visible spectrum or close to the visible spectrum. Indeed, polarization data in the NIR wavelength bands (beyond 1.0 μm) have not been widely measured nor utilized for aerosol retrievals. This paper evaluates the aerosol property information content obtained from a single-viewing satellite polarimetric measurements at 1,610 and 2,250 nm and investigates whether such measurements can be utilized in conjunction with shorter-wavelength bands (e.g., 490, 670, and 870 nm) to improve the retrieval of aerosol parameters over vegetated land. This work takes the heritage from the Dark Target (DT) algorithm (Kaufman, Wald, et al., 1997), in which the surface reflectance in the visible bands is approximately estimated from the measurement at 2,250 nm. The quantitative findings of this paper can further provide the important theoretical guidance for the development of next-generation polarimetric remote sensing platform sensors for the retrieval of aerosol properties (Ding et al., 2016; Dubovik et al., 2011).

Many of the past aerosol retrieval algorithms developed for single-viewing multispectral sensors, including the DT algorithm for Moderate Resolution Imaging Spectroradiometer (Kaufman, Wald, et al., 1997; Levy et al., 2007, 2010; Wang et al., 2017), the Deep Blue algorithm for Moderate Resolution Imaging Spectroradiometer and the Sea-Viewing Wide Field-of-View Sensor (Hsu et al., 2004, 2006), and the Ozone Monitoring Instrument retrieval algorithm in the ultraviolet band (Torres et al., 2007), typically avoided spectral bands with a high surface reflectance and focused instead on the retrieval of the AOD from bands with a low land surface reflectance. Similarly, the Bremen Aerosol Retrieval algorithm for the Medium Resolution Imaging Spectrometer dealt with the surface reflectance through the linear mixing of basic spectra for green vegetation and bare soil with the Normalized Difference Vegetation Index (NDVI; Santer et al., 1999; von Hoyningen-Huene et al., 2003). In contrast, the aerosol information content could increase significantly within multiangular measurements, thereby requiring a different type of aerosol retrieval algorithm, such as the dual-view retrieval algorithm for the Advance Along Track Scanning Radiometer (Sayer et al., 2012; Thomas et al., 2009) and the empirical orthogonal function algorithm for the Multiangle Imaging Spectroradiometer (Diner et al., 1998; Kahn et al., 2005; Martonchik et al., 2009).

The retrieval of aerosol properties from the airborne and spaceborne polarimetric measurements has rapidly gained interest over recent years. Previous studies have shown that the aerosol information content can be improved significantly with the use of measurements from additional wavelengths and viewing angles (Chowdhary et al., 2001; Hasekamp & Landgraf, 2005b; Knobelspiesse et al., 2011, 2012; Mishchenko et al., 2004; Mishchenko & Travis, 1997; Peralta et al., 2007; Waquet et al., 2007; Xu, van Harten, et al., 2017). For instance, polarimetric measurements at 443/490, 670, and 865 nm obtained using the polarized retrieval algorithm for the Polarization and Directionality of the Earth's Reflectance (POLDER) instrument can enhance the ability to retrieve various optical properties, especially for the fine-mode aerosols (Deuzé et al., 2000, 2001; Herman et al., 1997; Tanré et al., 2011; Zhang et al., 2016). The Multiviewing Channel Polarization Imager (3MI), which is a new polarimeter designed for the preparation of new-generation POLDER instrument and the airborne micropolarimeter (MICROPOL) prototype, employs two NIR polarized channels centered at 1.6 and 2.2 μm, and it is advantageously capable of the simultaneous inversion of multiple aerosol parameters (Goloub et al., 2003; Marbach et al., 2015; Waquet et al., 2005, 2007; Waquet, Cairns, et al., 2009). Other polarimeters include the Research Scanning Polarimeter and the Aerosol Polarimetry Sensor (Chowdhary et al., 2001; Knobelspiesse et al., 2011; Mishchenko et al., 2007; Peralta et al., 2007). Recently, another new spaceborne instrument known as the Polarized Scanning Atmospheric Corrector (PSAC), which was designed with multispectral single-viewing polarimetric measurements, was also developed in China to provide aerosol properties for the atmospheric corrections of other sensors onboard the same satellite. The airborne prototype of PSAC, namely, the Advanced Atmosphere Multiangle Polarization Radiometer, has been employed for some aerosol retrieval tests (Hou et al., 2015; Qie et al., 2015; Wang, Sun, et al., 2014; Wang et al., 2015).

Since increasing numbers of airborne and spaceborne sensors may have the ability to acquire polarimetric measurements at NIR wavelengths, several questions arise: (1) How many and what types of aerosol parameters can be simultaneously retrieved by adding NIR measurements? (2) To what extent can the retrieval errors be improved through the addition of NIR measurements? Addressing these two questions can provide theoretical guidance for the design of an aerosol inversion algorithm framework for real retrieval endeavors. However, a specific and comprehensive theoretical analysis of the information content analysis within these

NIR polarization measurements that support the development of an operational aerosol retrieval algorithm is still lacking. Therefore, this study focuses on single-viewing synthetic measurements of both the TOA radiance and the polarization at wavelengths of 490, 670, 870, 1,610, and 2,250 nm over vegetated land. Similar to the traditional DT algorithm, the 2,250 nm (scalar radiance/reflectance) band is quite useful for detecting densely vegetated surfaces, for which the ratio of the visible reflectance to the NIR reflectance in nearly constant (Kaufman, Wald, et al., 1997). Thus, we can assume that the surface reflectance at visible wavelengths (490 and 670 nm) can be approximately estimated from the TOA reflectance at 2,250 nm using a priori errors.

Over recent years, many studies have conducted analyses of the aerosol information content in satellite solar backscatter measurement in the ultraviolet to NIR spectral range by employing a variety of methods ranging from principal component analysis (Martynenko et al., 2010; Tanré et al., 1996; Veihelmann et al., 2007; Zubko et al., 2007) to the Shannon information content approach (Corradini & Cervino, 2006; Knobelspiesse et al., 2012; Lebsock et al., 2007) to the averaging kernel matrix technique (Chen, Wang, et al., 2017; Chen, Yang, et al., 2017; Frankenberg et al., 2012; Hasekamp & Landgraf, 2005b; Holzer-Popp et al., 2008; Hou et al., 2017; Xu & Wang, 2015). The number of degrees of freedom for signal (DFS) is generally used to represent the number of parameters that can be retrieved independently from TOA radiance/polarization measurements, provided that the surface reflectance and the a priori errors in the retrieval parameters can be characterized.

Following the optimal estimation framework (Rodgers, 2000), we have previously conducted information content analyses for new Aerosol Robotic Network (AERONET) polarimetric sensors and hyperspectral sensors (Hou et al., 2017; Xu & Wang, 2015); these analyses have further enabled the development of algorithms for AERONET polarimetric sensors (Xu et al., 2015). This study, however, is significantly different from our previous work, which neither utilized the intensity and polarization in NIR bands nor considered the surface polarized reflectance. Here building on the Unified Linearized Vector Radiative Transfer Model (UNL-VRTM; Wang, Xu, et al., 2014), we present new developments, including the integration of the combined surface contributions from the bidirectional reflectance distribution function (BRDF) and the bidirectional polarized reflectance distribution function (BPDF), for the generation of synthetic data for various scenarios containing different aerosol models, observation geometries, and wavelength combinations over vegetated land. We describe the model and methodology in section 2 and present our approach and experimental designs for the measurement simulations, and then we analyze synthetic data in section 3. Subsequently, we conduct an analysis on the aerosol information content and retrieval errors based on these synthetic measurements in section 4, after which we provide a summary of our findings and conclude our work in section 5.

2. Model and Methodology

2.1. Optimal Estimation and Information Content

Based on the optimal estimation theory (Hasekamp & Landgraf, 2005a; Rodgers, 2000), the forward model can be defined in the following form:

$$\mathbf{y} = \mathbf{F}(\mathbf{x}) + \boldsymbol{\epsilon}, \tag{1}$$

where $\mathbf{x} = [x_1, \ldots, x_n]^{\mathrm{T}}$ represents a state vector that containing n parameters to be retrieved, $\mathbf{y} = [y_1, \ldots, y_m]^{\mathrm{T}}$ represents an observation vector with m measurement elements, the superscript "T" represents a transpose operation, $\boldsymbol{\epsilon}$ is an experimental error term that includes observational noise and forward modeling uncertainties, and $\mathbf{F}$ denotes a forward model describing the physical relationship between $\mathbf{y}$ and $\mathbf{x}$ (here, it corresponds to the UNL-VRTM).

Under the assumption of a Gaussian distribution of errors, the scalar-valued cost function $J(\mathbf{x})$ can be constructed for an optimized inversion using the maximum likelihood method (Dubovik & King, 2000; Jeong et al., 2016; Waquet, Cairns, et al., 2009). Thus, the inversion problem can be represented as a nonlinear optimization problem as follows (Han et al., 2009; Hou et al., 2016; Sun et al., 2011):

$$\begin{aligned} &\min J(\mathbf{x}) \\ &\text{s.t. } \mathbf{l} \le \mathbf{x} \le \mathbf{u} \end{aligned}, \tag{2}$$

which means that the objective function $J(\mathbf{x})$ is optimized subject to (s. t.) the condition $\mathbf{l} \le \mathbf{x} \le \mathbf{u}$, where $\mathbf{l}$ and $\mathbf{u}$ represent the lower and upper bounds of the retrieval parameter vector $\mathbf{x}$, respectively. Among the many classical optimization algorithms, quasi-Newton methods are effective algorithms for constraining the local maximum and minimum of an objective function (Byrd et al., 1995; Sun et al., 2009; Yu et al., 2014; Zhu et al., 1994). When the optimal iteration of a quasi-Newton method converges under a predefined convergence accuracy, the retrieved stated vector $\widehat{\mathbf{x}}$ can be obtained.

An important metric for information content analysis is the averaging kernel matrix $\mathbf{A}$, which is defined as

$$\frac{\partial \widehat{\mathbf{x}}}{\partial \mathbf{x}} = \mathbf{A} = \left(\mathbf{K}^{\mathrm{T}}\mathbf{S}_{\epsilon}^{-1}\mathbf{K} + \mathbf{S}_{\mathrm{a}}^{-1}\right)^{-1}\mathbf{K}^{\mathrm{T}}\mathbf{S}_{\epsilon}^{-1}\mathbf{K}, \tag{3}$$

where the superscript "−1" represents an inverse operation of a matrix, $\mathbf{S}_{\epsilon}$ represents the covariance matrix of the error in both the measurements and the forward model, $\mathbf{S}_{\mathrm{a}}$ denotes the error covariance matrix for the a priori estimate $\mathbf{x}_{\mathrm{a}}$, and the Jacobian matrix $\mathbf{K}$ represents the partial derivatives of $\mathbf{F}(\mathbf{x})$ in equation (1) with respect to $\mathbf{x}$, the corresponding elements of which can be written in the form

$$\mathbf{K}_{j,i} = \frac{\partial y_j}{\partial x_i}, (i = 1, \ldots n; j = 1, \ldots, m). \tag{4}$$

This averaging kernel matrix characterizes the changes between the retrieved stated vector $\widehat{\mathbf{x}}$ and the true state vector $\mathbf{x}$ (Frankenberg et al., 2012; Xu & Wang, 2015), and the trace of $\mathbf{A}$, which is also known as the DFS, is equivalent to the number of independent pieces of information from the TOA measurements. Hence, the total DFS can be calculated as follows:

$$\text{Total DFS} = \text{Trace}(\mathbf{A}) = \sum\nolimits_{i=1}^{n} \mathbf{A}_{i,i}. \tag{5}$$

Correspondingly, the DFS of each individual retrieved parameter can be represented as

$$\text{DFS} = \frac{\partial \widehat{x}_i}{\partial x_i} = \mathbf{A}_{i,i}, \tag{6}$$

where the DFS result $\mathbf{A}_{i,\,i} = 1$ indicates that the observation is able to fully characterize the truth of x_i, while $\mathbf{A}_{i,\,i} = 0$ indicates that the observation is completely devoid of information on x_i. That is, values of $\mathbf{A}_{i,\,i}$ that are closer to 1 represent better retrievals of the parameter x_i; in contrast, values of $\mathbf{A}_{i,\,i}$ that are closer to 0 indicate a smaller information content from the retrieval of x_i. In addition, as long as the DFS result $\mathbf{A}_{i,\,i} > 0.5$ in this study, we can assume that the retrieval of the parameter x_i is successful.

The a posteriori error covariance matrix $\widehat{\mathbf{S}}$, which is another important metric, can be obtained by

$$\widehat{\mathbf{S}} = \left(\mathbf{K}^{\mathrm{T}}\mathbf{S}_{\epsilon}^{-1}\mathbf{K} + \mathbf{S}_{\mathrm{a}}^{-1}\right)^{-1}, \tag{7}$$

which means that the statistical uncertainties in the retrieved stated vector $\widehat{\mathbf{x}}$ are caused by measurement noise and the propagation of errors, while the square root of the diagonal elements (i.e., the propagation errors) are the posterior errors (i.e., the absolute errors). The observation error covariance matrix $\mathbf{S}_{\epsilon}$ can be written as

$$\mathbf{S}_{\boldsymbol{\epsilon}} = \mathbf{S}_{\mathbf{y}} + \mathbf{K}_{\mathbf{b}}\mathbf{S}_{\mathbf{b}}\mathbf{K}_{\mathbf{b}}^{\mathrm{T}}, \tag{8}$$

where $\mathbf{S}_{\mathbf{y}}$ denotes the measurement error covariance matrix, which accounts for the integrated effects of instrumental noise, radiometric calibration uncertainties, and additional polarimetric accuracy uncertainties (Waquet, Cairns, et al., 2009), and the expression $\mathbf{K}_{\mathbf{b}}\mathbf{S}_{\mathbf{b}}\mathbf{K}_{\mathbf{b}}^{\mathrm{T}}$ denotes the propagation errors in the forward model, where $\mathbf{S}_{\mathrm{b}}$ represents the error covariance matrix for a vector $\mathbf{b}$ in the forward model that is not contained within $\mathbf{x}$ but quantitatively influences the measurements, $\mathbf{K}_{\mathbf{b}}$ denotes the partial derivatives the measurements $\mathbf{y}$ with respect to the vector $\mathbf{b}$, and the elements have a similar format to those in equation (4). In addition, we assume that the errors are independent among the measurements, and the model errors for $\mathbf{b}$ are also noncorrelated; thus, both $\mathbf{S}_{\mathbf{y}}$ and $\mathbf{S}_{\mathbf{b}}$ can be regarded as diagonal matrices (Dubovik et al., 2000).

2.2. Forward Model and Observation Vector

We use UNL-VRTM as the forward model for the simulation of the synthetic measurements. UNL-VRTM was specifically designed for the simulation of atmospheric remote sensing observations and for the inversion

Table 1
The List of Scenarios of Satellite Observations Used for the Information Content Analysis

Scenario	Single observations included	Expected application sensors
P1	*Q* and *U* at 490, 670, and 870 nm	POLDER/PARASOL (Deuzé et al., 2001)
P2	*Q* and *U* at 490, 670, 870, and 1,610 nm	Chinese AMPR (Qie et al., 2015)
P3	*Q* and *U* at 490, 670, 870, 1,610, and 2,250 nm	MICROPOL (Waquet, Cairns, et al., 2009)
P4	Scenario P3 plus *I* at 490 and 670 nm	Chinese PSAC

Note. AMPR, Advanced Atmosphere Multiangle Polarization Radiometer; PARASOL, Polarization and Anisotropy of Reflectances for Atmospheric Science coupled with Observations from a Lidar.

of aerosol, gas, cloud, and/or surface properties from these observations (www.unl-vrtm.com; Wang, Xu, et al., 2014). It comprises VLIDORT (Spurr, 2006) for radiative transfer, linearized Mie and linearized T-matrix code (Spurr et al., 2012) for aerosol single scattering, a Rayleigh scattering module, line-by-line gas absorption calculations using the HITRAN database, and a BRDF and BPDF module (Spurr, 2004) for characterizing the surface properties. The outputs of UNL-VRTM include not only full elements of the Stokes vector but also their sensitivities (i.e., Jacobians) with respect to various parameters that are relevant to the aerosol microphysics and optical properties, gas absorption, and surface properties. UNL-VRTM has also been widely used to study information contents and develop inversion algorithm for the retrieval of aerosols and surface properties from various measurements (Chen, Wang, et al., 2017; Ding et al., 2016; Hou et al., 2016, 2017; Wang et al., 2016; Xu et al., 2015; Xu, Wang, Wang, Henze, et al., 2017; Xu, Wang, Wang, Zeng, et al., 2017; Xu & Wang, 2015).

Based on light scattering theory, the four-vector $\boldsymbol{I}$ is usually utilized to represent the diffuse field of Stokes components $\{I, Q, U, V\}$, in which the element I denotes the total intensity (i.e., radiance), Q and U both describe the linearly polarized radiation, and V characterizes circularly polarized radiation (Spurr, 2006). Since V is typically very small relative to the other three elements, we exclude V hereafter in this study.

As listed in Table 1, we consider four observation scenarios to analyze the information contributions from the measurements of different sensors. In the first scenario (P1), we consider only the polarized radiances Q and U at 490, 670, and 870 nm corresponding to the POLDER/Polarization and Anisotropy of Reflectances for Atmospheric Science coupled with Observations from a Lidar instrument (Deuzé et al., 2000, 2001), and the 490 nm band is used instead of 443 nm (Tanré et al., 2011). Polarimetric measurements at 1,610 nm are added to the second scenario (P2) to represent the airborne Advanced Atmosphere Multiangle Polarization Radiometer instrument (Qie et al., 2015). Next, the third scenario (P3) is defined identical to scenario P2 in addition to polarimetric measurements at 2,250 nm to represent the MICROPOL instrument (Goloub et al., 2003; Waquet et al., 2005; Waquet, Cairns, et al., 2009). Finally, the fourth scenario (P4) is defined to further include TOA radiance measurements I at 490 and 670 nm to represent the PSAC instrument by considering the scalar radiance measurements. The reason for including only the radiances at 490 and 670 nm is that the surface reflectances in these two bands could be approximately derived from the TOA reflectance at 2,250 nm over vegetated land (Kaufman, Wald, et al., 1997). Meanwhile, the relationships among the other bands (e.g., 870 and 1,610 nm) with respect to the 2,250 nm have not been intensively studied.

Therefore, the number of elements in the measurement vector $\mathbf{y}$ depends on the selected scenario:

$$\mathbf{y} \in [I_{\lambda_1}, I_{\lambda_2}, Q_{\lambda_1}, \ldots, Q_{\lambda_5}, U_{\lambda_1}, \ldots, U_{\lambda_5}]^{\mathrm{T}}, \tag{9}$$

where λ_1 through λ_5 successively represent the 490, 670, 870, 1,610, and 2,250 nm wavelength bands. These representations are employed hereafter throughout this paper. As a result, the observation vectors in scenarios P1, P2, P3, and P4 contain 6, 8, 10, and 12 observations, respectively.

2.3. Aerosol Model

This study characterizes aerosol properties for up to five pairs of parameters for both fine- and coarse-mode aerosol particles. These five pairs of parameters are the columnar volume concentrations V_0^{f} and V_0^{c}, the effective radii $r_{\mathrm{eff}}^{\mathrm{f}}$ and $r_{\mathrm{eff}}^{\mathrm{c}}$, the effective variances $v_{\mathrm{eff}}^{\mathrm{f}}$ and $v_{\mathrm{eff}}^{\mathrm{c}}$, and the real (subscript "r") and imaginary (subscript "i")

parts m_r^f, m_i^f, m_r^c, and m_i^c of the complex refractive indices at 550 nm, where the superscripts "f" and "c" represent the fine- and coarse-mode particles, respectively.

A bimodal lognormal function is typically used to describe the particle size distribution of spherical aerosol particles. Thus, we employ r_{eff} and v_{eff} as the input parameters for the simulations using UNL-VRTM (Xu & Wang, 2015). Hence, the total aerosol volume (V_0 in units of $\mu m^3 \mu m^{-2}$) and the volumetric fine-mode fraction (FMF_V) can be defined as

$$\begin{cases} V_0 = V_0^f + V_0^c \\ FMF_V = V_0^f / V_0 \end{cases}. \tag{10}$$

Correspondingly, the AOD (τ_a) at the wavelength λ can be derived from V_0^f and V_0^c (Xu et al., 2013):

$$\tau_a = \tau_a^f + \tau_a^c = \frac{3V_0^f}{4r_{eff}^f} Q_{ext}^f + \frac{3V_0^c}{4r_{eff}^c} Q_{ext}^c, \tag{11}$$

and the FMF of the AOD (Kleidman et al., 2005; Ramachandran, 2007; Yu et al., 2009) can be written as

$$FMF = \tau_a^f / \tau_a, \tag{12}$$

where Q_{ext} is the extinction efficiency factor (i.e., the ratio of the extinction cross section to the geometric cross section) and τ_a^f and τ_a^c represent the fine-mode and coarse-mode AODs, respectively. Therefore, the wavelength-independent V_0^f and V_0^c are usually contained within the framework of the information content analysis and aerosol retrieval instead of varied AOD and FMF along the wavelength.

Furthermore, the complex refractive indices of the aerosols also vary along with the wavelength. To parameterize this spectral dependence, we introduce a power-law relationship as follows (Dubovik & King, 2000):

$$\begin{cases} m_r(\lambda) = m_r(\lambda_0) \left(\frac{\lambda}{\lambda_0}\right)^{-b_r} \\ m_i(\lambda) = m_i(\lambda_0) \left(\frac{\lambda}{\lambda_0}\right)^{-b_i} \end{cases}. \tag{13}$$

where $m_r(\lambda_0)$, b_r, $m_i(\lambda_0)$, and b_i are the coefficients, λ_0 denotes the reference wavelength, and the subscripts "r" and "i" denote the real and imaginary parts of the refractive indices, respectively. In this study, we set the reference wavelength λ_0 = 550 nm, and thus, $m_r(\lambda_0)$ and $m_i(\lambda_0)$ correspond to the refractive index at 550 nm. The Jacobian expressions for $m_r(\lambda_0)$, $m_i(\lambda_0)$, b_r, and b_i can then be further obtained (Hou et al., 2017). Hereafter, we use the symbols m_r and m_i to represent the refractive indices $m_r(\lambda_0)$ and $m_i(\lambda_0)$, respectively, at the reference wavelength of with λ_0 = 550 nm in this paper.

2.4. Surface Model

For the UNL-VRTM forward model, the land surface reflectance matrix $\boldsymbol{R}$ can be represented as a sum of numerous surface reflection phenomena as follows:

$$\boldsymbol{R}(\theta_0, \theta_v, \phi, \lambda) = r_\lambda \begin{bmatrix} 1 & 0 & 0 & 0 \\ 0 & 0 & 0 & 0 \\ 0 & 0 & 0 & 0 \\ 0 & 0 & 0 & 0 \end{bmatrix} + \frac{\rho_{Maignan}}{2} \begin{bmatrix} r_i^2 + r_r^2 & r_i^2 - r_r^2 & 0 & 0 \\ r_i^2 - r_r^2 & r_i^2 + r_r^2 & 0 & 0 \\ 0 & 0 & 2r_i r_r & 0 \\ 0 & 0 & 0 & 2r_i r_r \end{bmatrix}. \tag{14}$$

where θ_0 and θ_v represent the solar zenith angle and viewing zenith angle, respectively, the relative azimuth angle ϕ is defined by the solar azimuth angle ϕ_0 and viewing azimuth angle ϕ_v, r_λ represents the formulation of the BPDF at the wavelength λ, $\rho_{Maignan}$ represents the empirical coefficients of the BPDF developed by Maignan et al. (2009), and the matrix in the second part of equation (14) corresponds to the Fresnel reflection matrix $\mathbf{F}(\gamma, n_i)$, in which the definition of the coefficients r_r and r_i are the same as those in the work of Dubovik et al. (2011).

An assumed Lambertian reflectance is deemed sufficient to describe the contribution from the surface reflectance because a single observation is considered in this study. However, to assess the influences of different observations on the information content within the aerosol retrieval, we still consider the BRDF model in the

Table 2
The Aerosol Parameters for Fine- and Coarse-Mode Aerosol Particles

Mode	r_{eff} (μm)	v_{eff}	m_r (550 nm)	m_i (550 nm)	b_r	b_i
Fine	0.21 (80%)	0.25 (80%)	1.434 (0.15)	0.011 (0.01)	0.016 (80%)	−0.266 (80%)
Coarse	1.90 (80%)	0.41 (80%)	1.549 (0.15)	0.003 (0.005)	0.017 (80%)	0.625 (80%)

Note. r_{eff} and v_{eff} represent the effective radius and effective variance, respectively, m_r and m_i represent the real and imaginary parts of the complex refractive indices, respectively, and b_r and b_i represent the coefficients of the wavelength-dependent complex refractive indices in equation (13). Bracketed data represent a priori errors corresponding to the parameters.

forward simulations. The kernel-driven BRDF model for the surface reflectance integrated within UNL-VRTM can be given as

$$r_\lambda(\theta_0, \theta_v, \phi) = f_{iso}(\lambda) + k_1(\lambda) f_{geom}(\theta_0, \theta_v, \phi) + k_2(\lambda) f_{vol}(\theta_0, \theta_v, \phi), \tag{15}$$

where f_{iso}, f_{geom}, and f_{vol} respectively represent the isotropic, geometric-optical, and volumetric surface scattering, and the corresponding variables $f_{iso}(\lambda)$, $k_1(\lambda)$, and $k_2(\lambda)$ are the coefficients of the BRDF kernels at the wavelength λ (Roujean et al., 1992; Wanner et al., 1995; Strahler et al., 1997). For the simulation of the radiances at 490 and 670 nm, we assume that the surface reflectances in these two visible bands can be approximately derived from the TOA reflectance at 2,250 nm (Kaufman, Wald, et al., 1997), and the a priori errors in r_λ are set to 40% to encompass the uncertainties in the empirical relationships and the influences of aerosols at 2,250 nm.

For the contribution from the surface polarized reflectance, a BPDF model has also been integrated in UNL-VRTM as follows:

$$R_p^s(\theta_0, \theta_v, \phi) = \rho_{Maignan} \mathbf{F}_{1,2}(\gamma, n_i), \tag{16}$$

in which

$$\rho_{Maignan} = \frac{C \exp(-\tan\gamma) \exp(-NDVI)}{4(\cos\theta_0 + \cos\theta_V)}, \tag{17}$$

where $\mathbf{F}_{1,2}(\gamma, n_i)$ represents the polarized component of the Fresnel reflection matrix $\mathbf{F}(\gamma, n_i)$, n_i is the reflective index of vegetative matter (usually set to 1.5), and γ denotes one half of the phase angle, which is supplementary to the scattering angle. In addition, the NDVI is usually defined by two radiance measurements from one visible and one infrared wavelength band (Spurr, 2012). Furthermore, C is the only free linear parameter in this model, and it depends on the surface type (Maignan et al., 2009). Because the surface polarized reflectance R_p^s can be regarded as independent of the wavelength (Waquet, Léon, et al., 2009), we consider only retrieving the parameter C for the BPDF in equation (17) simultaneously with the aerosol parameters. For vegetated surfaces, we follow the parameter determinations obtained from airborne multiangle photopolarimetric measurements (Litvinov et al., 2011) and set C = 6.57 and NDVI = 0.62 for the polarized simulations using UNL-VRTM.

2.5. Definition of A Priori Errors

For the information content analysis of the total DFS in the aerosol retrieval, the state vector can be defined as

$$\mathbf{x} = \left[V_0^f, V_0^c, m_r^f, m_i^f, m_r^c, m_i^c, r_{eff}^f, v_{eff}^f, r_{eff}^c, v_{eff}^c, C\right]^T, \tag{18}$$

where the parameters b_r^f, b_i^f, b_r^c and b_i^c, are not contained in $\mathbf{x}$, because we consider only retrieving the refractive index at 550 nm. Correspondingly, the error matrix of the state vector follows our previous work (Hou et al., 2016, 2017):

$$\mathbf{S}_a = \mathrm{diag}\left(\left[\sigma^2_{V_0^f}, \sigma^2_{V_0^c}, \sigma^2_{m_r^f}, \sigma^2_{m_i^f}, \sigma^2_{m_r^c}, \sigma^2_{m_i^c}, \sigma^2_{r_{eff}^f}, \sigma^2_{v_{eff}^f}, \sigma^2_{r_{eff}^c}, \sigma^2_{v_{eff}^c}, \sigma^2_C\right]^T\right), \tag{19}$$

where the function diag represents the assignment of vectors along the main diagonal of a matrix. The corresponding a priori errors in the aerosol parameters for fine- and coarse-mode particles are included in Table 2 in brackets, and the a priori errors in V_0 are given in Table 3 in brackets, all of which are based on the climatological statistics of aerosol properties from AERONET (Xu et al., 2015; Xu & Wang, 2015). In addition, we assume that the a priori errors in the aerosol parameters shown in Tables 2 and 3 are mutually

Table 3
The Aerosol Scenarios for the Simulations

Scenarios	V_0 ($\mu m^3 \mu m^{-2}$)	FMF_V	τ_a (550 nm)	AE	SSA (550 nm)
Fine-dominated	0.149 (80%)	0.8	0.8	1.50	0.94
Coarse-dominated	0.394 (80%)	0.2	0.8	0.82	0.92

Note. V_0, FMF_V, τ_a, AE, and SSA represent the columnar volume concentration, volume fine-mode fraction, AOD, Ångström exponent, and single scatter albedo, respectively. Bracketed data represent a priori errors corresponding to the parameters.

independent of each other, and thus, the error matrix $\mathbf{S}_a$ can be simplified as a diagonal matrix in equation (19). In addition, the a priori errors in the parameter C of the BPDF, which are assumed to be 40% by following the work of Maignan et al. (2009), are listed in Table 4.

Under the assumption that the errors are independent among the single-viewing measurements of equation (9), the measurement error covariance matrix can also be presented in a diagonal form as follows:

$$\mathbf{S}_y \in \mathrm{diag}\left(\left[\left(e_{y_i} I_{\lambda_1}\right)^2, \ldots, \left(e_{y_i} Q_{\lambda_1}\right)^2, \ldots, \left(e_{y_i} U_{\lambda_1}\right)^2, \ldots\right]^T\right), \tag{20}$$

where e_{y_i} represents the relative error in the polarimetric measurements at each wavelength corresponding to the scenarios listed in Table 1, $i = 1, \ldots, m$, and m denotes the number of elements in the observation vector. By considering the integrated effects of instrumental noise with radiometric calibration and polarimetric accuracy uncertainties, e_{y_i} is set to 5% for both the radiance and the polarization in this study for the information content analysis.

The vector $\mathbf{b}$ consisting of forward simulations that are not contained in $\mathbf{x}$ but quantitatively influence the TOA radiance measurements is defined as

$$\mathbf{b} \in \left\{b_r^f, b_i^f, b_r^c, b_i^c, r_{\lambda_1}, r_{\lambda_2}\right\}, \tag{21}$$

and the error matrix is as follows:

$$\mathbf{S_b} \in \mathrm{diag}\left(\left[\sigma^2_{b_r^f}, \sigma^2_{b_i^f}, \sigma^2_{b_r^c}, \sigma^2_{b_i^c}, \sigma^2_{r_{\lambda_1}}, \sigma^2_{r_{\lambda_2}}\right]^T\right). \tag{22}$$

Here we have to consider only the propagation of errors in the surface reflectances for scenario P4, and we set the a priori errors to 40% as listed in Table 4 by following the work of Kaufman, Wald, et al. (1997).

Due to an insufficient number of single-angle observations, these 10 aerosol parameters cannot be retrieved simultaneously; thus, we must select some parameters to separately retrieve fine- and coarse-dominated aerosols based on an analysis of their individual information contents, which will be discussed in detail in the next section. Accordingly, for fine-dominated aerosols, the state vector contains only six aerosol elements and one BPDF parameter:

$$\mathbf{x} = \left[V_0^f, V_0^c, m_r^f, m_i^f, r_{\mathrm{eff}}^f, r_{\mathrm{eff}}^c, C\right]^T, \tag{23}$$

in which

$$\mathbf{b} \in \left\{b_r^f, b_i^f, m_r^c, m_i^c, b_r^c, b_i^c, v_{\mathrm{eff}}^f, v_{\mathrm{eff}}^c, r_{\lambda_1}, r_{\lambda_2}\right\}. \tag{24}$$

Table 4
The BRDF/BPDF Coefficients and A Priori Errors for a Vegetated Surface

Model	Wavelength	$f_{iso}(\lambda)$	$k_1(\lambda)$	$k_2(\lambda)$	C	A priori errors
BRDF	490 nm	0.041	0.011	0.010	—	40%
	670 nm	0.064	0.018	0.012	—	40%
BPDF	490–2,250 nm	—	—	—	6.57	40%

Note. $f_{iso}(\lambda)$, $k_1(\lambda)$, and $k_2(\lambda)$ represent the coefficients of the Lambertian, Ross-thick, and Li-sparse kernels of the BRDF model at the wavelength λ in equation (15), respectively, and C is the linear parameter of the BPDF in equation (17).

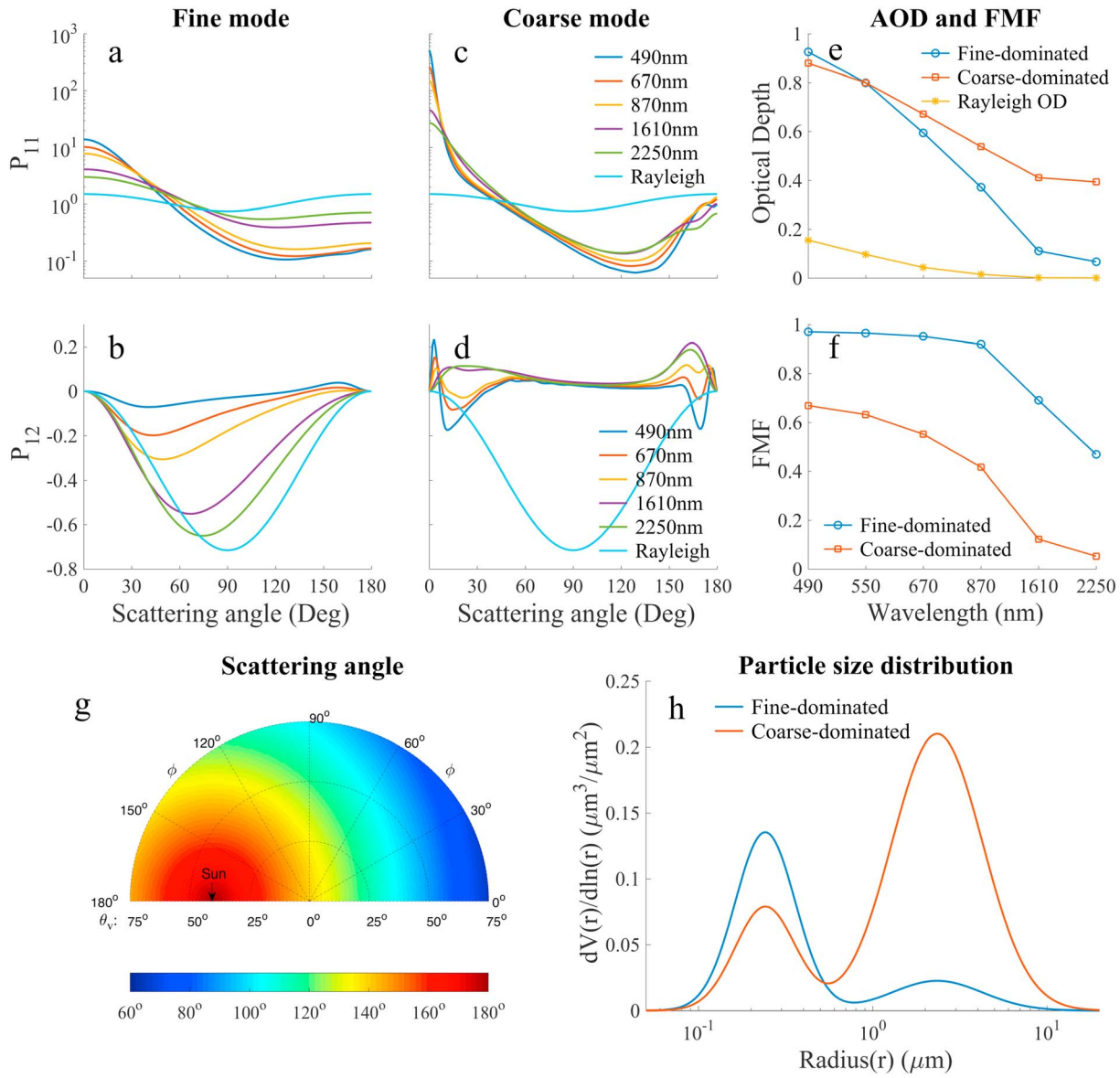

Figure 1. (a, c) The scattering phase function P_{11} and (b, d) the polarized phase function P_{12} as functions of the scattering angles at each wavelength for the fine- and coarse-mode aerosol models, respectively, adopted for the information content analysis as well as the (e) AODs and (f) FMFs as a function of the wavelength for the fine- and coarse-dominated aerosol scenarios with (h) their corresponding particle size distributions. In addition, the phase functions and optical depths (ODs) of molecules via Rayleigh scattering are included in Figures 1a–1e. (g) The polar plot of scattering angles along the viewing zenith angles θ_v and relative azimuth angles ϕ with a solar zenith angle of θ_0=40° used for the simulations in this study is dispalyed. In this polar plot, the radius denotes a change in θ_v from 0° to 75°, and the polar angle ϕ represents a change from 0° to 180°; when ϕ = 180°, this geometry indicates that the observer and the Sun face the same direction and are located on the same side of the main plane, and this convention is used for the other polar plots in this paper.

Meanwhile, for the coarse-dominated aerosols, the state vector also includes only six aerosol elements with a BPDF parameter:

$$\mathbf{x} = \left[V_0^{\mathrm{f}}, V_0^{\mathrm{c}}, m_{\mathrm{r}}^{\mathrm{c}}, m_{\mathrm{i}}^{\mathrm{c}}, r_{\mathrm{eff}}^{\mathrm{f}}, r_{\mathrm{eff}}^{\mathrm{c}}, C\right]^{\mathsf{T}}, \tag{25}$$

in which

$$\mathbf{b} \in \left\{b_{\mathrm{r}}^{\mathrm{f}}, b_{\mathrm{i}}^{\mathrm{f}}, m_{\mathrm{r}}^{\mathrm{f}}, m_{\mathrm{i}}^{\mathrm{f}}, b_{\mathrm{r}}^{\mathrm{c}}, b_{\mathrm{i}}^{\mathrm{c}}, v_{\mathrm{eff}}^{\mathrm{f}}, v_{\mathrm{eff}}^{\mathrm{c}}, r_{\lambda_1}, r_{\lambda_2}\right\}. \tag{26}$$

For the calculation of the information contents using these selected aerosol parameters, the AERONET retrieval errors (Dubovik et al., 2000) can be employed for the a priori errors in the predefined aerosol parameters (i.e., $r_{\text{eff}}^{\text{f}}, v_{\text{eff}}^{\text{f}}, r_{\text{eff}}^{\text{c}}, v_{\text{eff}}^{\text{c}}, m_{\text{r}}^{\text{c}}$, and m_{i}^{c}) in the vector **b** used to define the error matrix $\mathbf{S_b}$.

3. Synthetic Data and Simulated Results

To obtain the synthetic data using UNL-VRTM for the information content analysis, different observation geometries are considered with various solar zenith angles (θ_0), viewing zenith angles ($\theta_{\text{v}} = 0° - 75°$ with a step of 1°) and relative azimuth angles ($\phi = 0° - 180°$ with a step of 1°). The TOA synthetic data are calculated using UNL-VRTM for a midlatitude summer atmospheric profile for both fine-dominated and coarse-dominated aerosol cases (as listed in Table 3). In both cases, the aerosols are mixed with different relative percentages of fine- and coarse-mode particles. The parameters of the particle size distributions and refractive indices for the fine- and coarse-mode aerosols are taken from our previous work (Hou et al., 2017; Xu & Wang, 2015) and are listed in Table 2. The fine-mode $r_{\text{eff}}^{\text{f}}$ and $v_{\text{eff}}^{\text{f}}$ parameters are chosen to represent sulfate aerosols at a relative humidity of 60% (Drury et al., 2010; Hess et al., 1998), and the fine-mode refractive indices m_{r}^{f} and m_{i}^{f} are based on a climatological analysis using multiyear AERONET inversion products over Beijing, as the values are consistent with those in Figure 2 of Xu et al. (2015). Meanwhile, the corresponding values for coarse-mode aerosols are derived from the research on large spherical particles (Patterson et al., 1977; Wagner et al., 2012). Specifically, we employ two different AODs of 0.2 and 0.8 at 550 nm to represent the clear and polluted aerosol loadings, respectively (Hou et al., 2017). Thus, for τ_{a}= 0.8 at 550 nm, V_0 can vary from 0.149 to 0.394 $\mu\text{m}^3\mu\text{m}^{-2}$ with FMF_{V} varying from 0.2 to 0.8 for the fine-dominated and coarse-dominated aerosol scenarios, respectively. Correspondingly, the values of V_{total} for other AODs, such as the τ_{a}= 0.2 case, can be obtained via linear scaling.

Figure 1 shows the scattering phase function (P_{11}) and the polarized phase function (P_{12}) for the selected aerosol models and Rayleigh scattering as well as the corresponding AODs, Rayleigh optical depths, and FMFs as a function of the wavelength for the fine- and coarse-dominated aerosol scenarios with their corresponding particle size distributions. In addition, polar plots of the scattering angle (Θ) along the viewing zenith angles θ_{v} and relative azimuth angles ϕ with a solar zenith angle of θ_0=40° are also illustrated corresponding to both P_{11} and P_{12}. Here the calculations of the aerosol single scattering properties, including the phase functions P_{11} and P_{12}, are performed using the linearized Mie scattering electromagnetic code integrated in UNL-VRTM for spherical particles (Mishchenko & Travis, 1998; Spurr et al., 2012). The fine- and coarse-mode aerosols exhibit distinct differences between the phase functions P_{11} and P_{12} with, for example, the spectral dependency of extinction and the single scattering albedo (SSA). These distinct scattering signatures obtained by integrating aerosols and molecules (Rayleigh scattering in the visible bands) can be manifested as unique fingerprints in the TOA radiances and polarizations of different bands detected by satellite sensors. Following this principle, the addition of channels will likely introduce more independent mode-resolved aerosol information, and thus, additional aerosol microphysical properties can probably be retrieved by adding the NIR wavelength bands.

Figures 2a–2b illustrate a polar plot of the simulated BRDF results at 490 and 670 nm, and Figure 2c shows the polar plot results for the BPDF, which is assumed to be independent of the wavelength. The simulations are conducted with a solar zenith angle of $\theta_0 = 40°$ with the same color bar. For the BRDF results over vegetated surfaces, the surface reflectances at large scattering angles ($\Theta > 160°$) around the region of $\theta_{\text{v}} = \theta_0$ and $\phi = 180°$, which has been called a BRDF hotspot by many previous study (Chen & Cihlar, 1997; Gatebe & King, 2016), are much stronger than those of other geometries. In contrast, the backscattering polarized reflectance of the vegetated BPDF is much smaller than that for the forward-scattering polarized reflectance; thus, the BPDF is smaller for larger scattering angles, which is consistent with the previous research regarding the BPDF model (Breon & Maignan, 2017; Maignan et al., 2009).

With respect to the BPDF model free linear parameter C at 670 nm in Figure 2c, Figures 2d–2f illustrate the polar plots of the Jacobians for the simulated TOA I, Q, and U for fine-dominated aerosols. The magnitudes of $\frac{\partial I}{\partial C}$, $\frac{\partial Q}{\partial C}$, and $\frac{\partial I}{\partial C}$ are approximately $10^{-3} - 10^{-2}$, $10^{-4} - 10^{-5}$, and $10^{-5} - 10^{-6}$, respectively, and the Jacobians (i.e., the sensitivity) of the radiance I with respect to C is at least two orders of magnitudes larger than the Jacobians of both Q and U. That is, the radiance I is not only influenced by the free linear

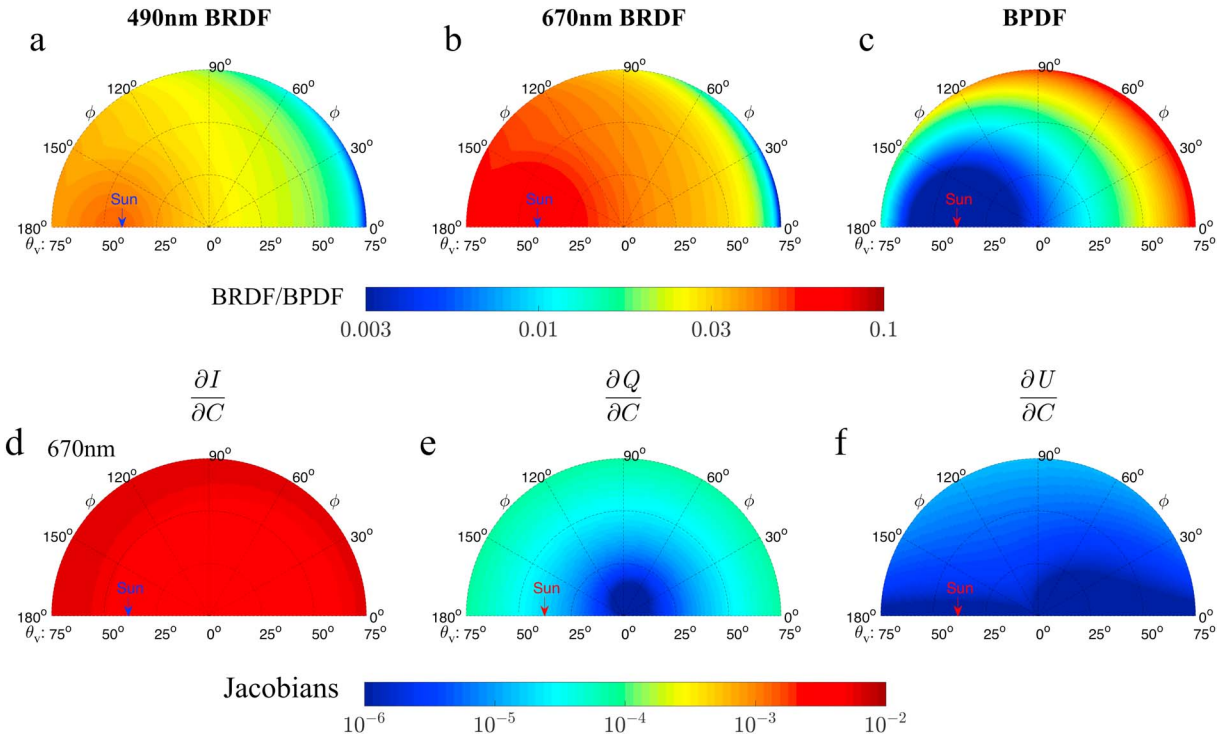

Figure 2. The polar plots of the angular distribution of the BRDF and BPDF models for a vegetated surface as well as the angular distributions of the Jacobians of the simulated TOA polarimetric measurements with respect to the BPDF parameter *C*. (a, b) The BRDF results at 490 nm and 670 nm, respectively, are shown. (c) The BPDF results are displayed, which are spectrally independent. (d)–(f) The results of $\frac{\partial I}{\partial C}$, $\frac{\partial Q}{\partial C}$, and $\frac{\partial I}{\partial C}$ at 670 nm with an AOD of $\tau_a = 0.8$ for fine-dominated aerosols. The simulations are performed at a solar zenith angle of 40°, and the polar coordinates are defined similar to Figure 1g.

parameter *C* but also contains more information of the BPDF model than either *Q* or *U*, and therefore, radiance measurements cannot be ignored during the retrieval of the BPDP parameter, which will be discussed in detail later. Meanwhile, the Jacobians for the other wavelength bands and other aerosol models have similar polar plots, and the results of which are not shown here.

To compare the simulated TOA results based on the predefined BRDF and BPDF among the different bands, we first provide definitions of the TOA reflectance R^{TOA} and the polarized reflectance $R_{\mathrm{p}}^{\mathrm{TOA}}$ as follows (Qie et al., 2015):

$$R^{\mathrm{TOA}} = \frac{\pi I}{\cos(\theta_0)E_0}, \quad R_{\mathrm{p}}^{\mathrm{TOA}} = \frac{\pi\sqrt{Q^2+U^2}}{\cos(\theta_0)E_0}. \tag{27}$$

where E_0 represents the extraterrestrial spectral solar irradiance. In general, TOA measurement results mainly depend on Rayleigh scattering, aerosol contributions (both scattering and absorption), surface contributions, and gas absorption (Dubovik et al., 2011; Kaufman, Tanré, et al., 1997; King et al., 1999; Waquet, Cairns, et al., 2009). That is, the results of R^{TOA} and $R_{\mathrm{p}}^{\mathrm{TOA}}$ are determined by the integrated contribution from the AOD, the SSA, the phase functions P_{11} and P_{12} for the mixing of molecules and aerosols within the atmospheric window (Spurr, 2006), and the surface reflectance and polarized surface reflectance (Dubovik et al., 2011).

Figure 3 shows the polar plot of R^{TOA} in the 490 and 670 nm bands for fine- and coarse-dominated aerosols, respectively, as well as the mean value of R^{TOA} (within an adjacent 10° range) as a function of the scattering angle ranging from 60° to 180° at a step of 10°. Although the AOD at 550 nm and the surface models for the foreward simulations are identical, the polar-plot distributions of R^{TOA} for the two different aerosol models (i.e., for fine- and coarse-dominated aerosols) still exhibit notable differences because of their different scattering phase functions and SSAs. As observed in Figures 3c and 3f, the mean TOA reflectance R^{TOA} in the visible bands gradually decreases with an increase in the scattering angles Θ from 60° to 140° and reaches a minimum at Θ = 140°, after which the mean value of R^{TOA} increases with an increase in the scattering angle

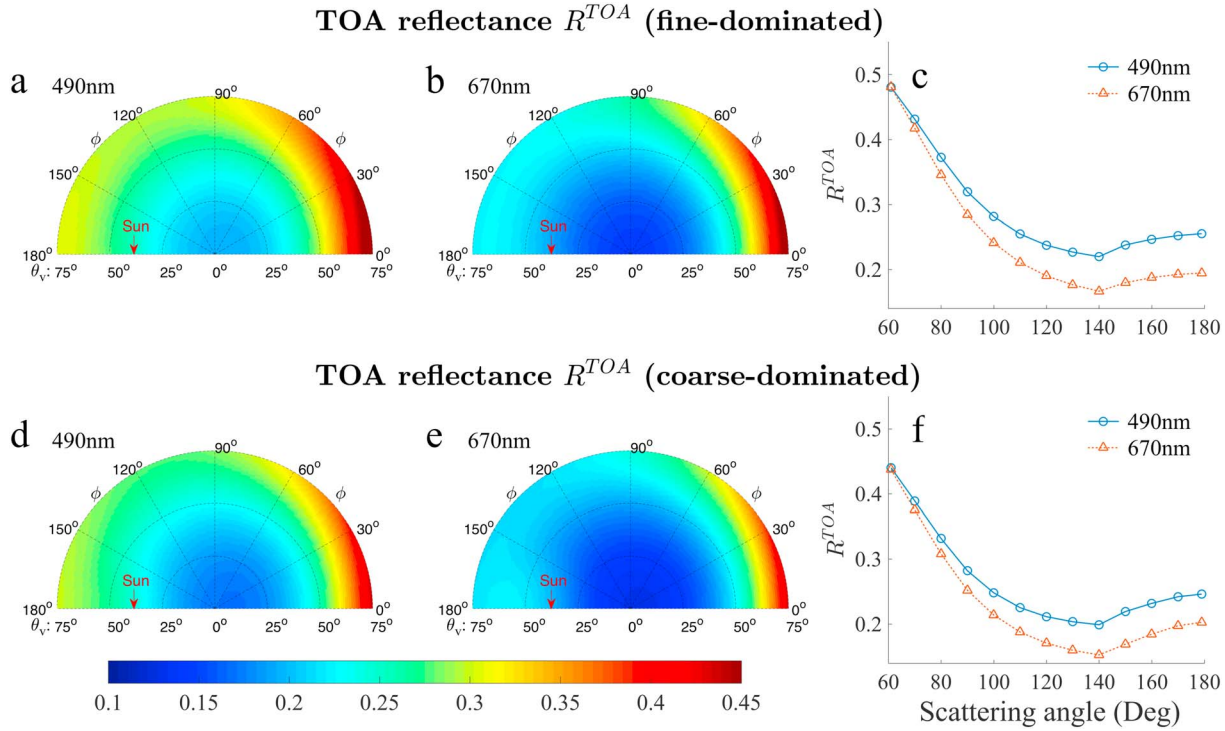

Figure 3. The polar-plot of the TOA reflectance R^{TOA} based on the BRDF model shown in Figure 2 at (a, d) 490 nm and (b, e) 670 nm using the same color bar as well as (c, f) the mean value of R^{TOA} (within an adjacent 10° range) as a function of the scattering angle ranging from 60° to 180° with a step of 10°. The upper panels and lower panels show the results for fine-dominated and coarse-dominated aerosols, respectively, with an AOD of τ_a = 0.8. The polar coordinates are defined similar to Figure 2.

in approximate agreement with the shape of P_{11} along the scattering angle. In addition, the results of R^{TOA} at 490 nm are larger than those at 670 nm due to the more significant contribution from Rayleigh scattering.

Figure 4 illustrates the polar plots of the TOA polarized reflectance R_p^{TOA} at the 490, 670, 870, 1,610, and 2,250 nm with the same color bars for fine- and coarse-dominated cases as well as the mean value of R_p^{TOA} (within an adjacent 5° range) as a function of the scattering angle ranging from 60° to 180° with a step of 5°. The R_p^{TOA} values mainly decrease with an increase in the scattering angles at 490, 670, and 870 nm both for fine- and coarse-dominated aerosols; the behavior is mainly the product of the integrated contributions from the surface polarized reflectance, molecules, and aerosols (Deuzé et al., 2001; Xie et al., 2013). Meanwhile, because the contribution from Rayleigh scattering can be ignored at the NIR wavelength bands (e.g., 1,610 and 2,250 nm), the R_p^{TOA} values are influenced only by the contributions from the surface polarized reflectance and aerosols. In contrast with the R_p^{TOA} curve along Θ for the fine-dominated case as shown in Figure 4f, an apparent peak in the R_p^{TOA} curve in the scattering angle range of $140° < \Theta < 180°$ is observed at 1,610 and 2,250 nm for the coarse-dominated aerosols as shown in Figure 4l, and this curve corresponds to the shape of the polarized phase function along Θ shown in Figure 1b (Waquet et al., 2007; Waquet, Cairns, et al., 2009). Therefore, information regarding coarse-mode aerosols such as dust could be detected more effectively using polarimetric measurements at 1,610 and 2,250 nm when Θ is in the range between 140° and 180°.

4. Information Content Analysis Results

4.1. Total DFS of the Aerosol Retrieval

Figure 5 shows polar plots of the total DFS angular distribution of the 10 retrieved aerosol parameters of equation (18) with different viewing zenith angles (θ_v = 0° – 75°) and relative azimuth angles (ϕ = 0° – 180°), and the observation scenarios P1 through P4 are considered for both fine- and coarse-

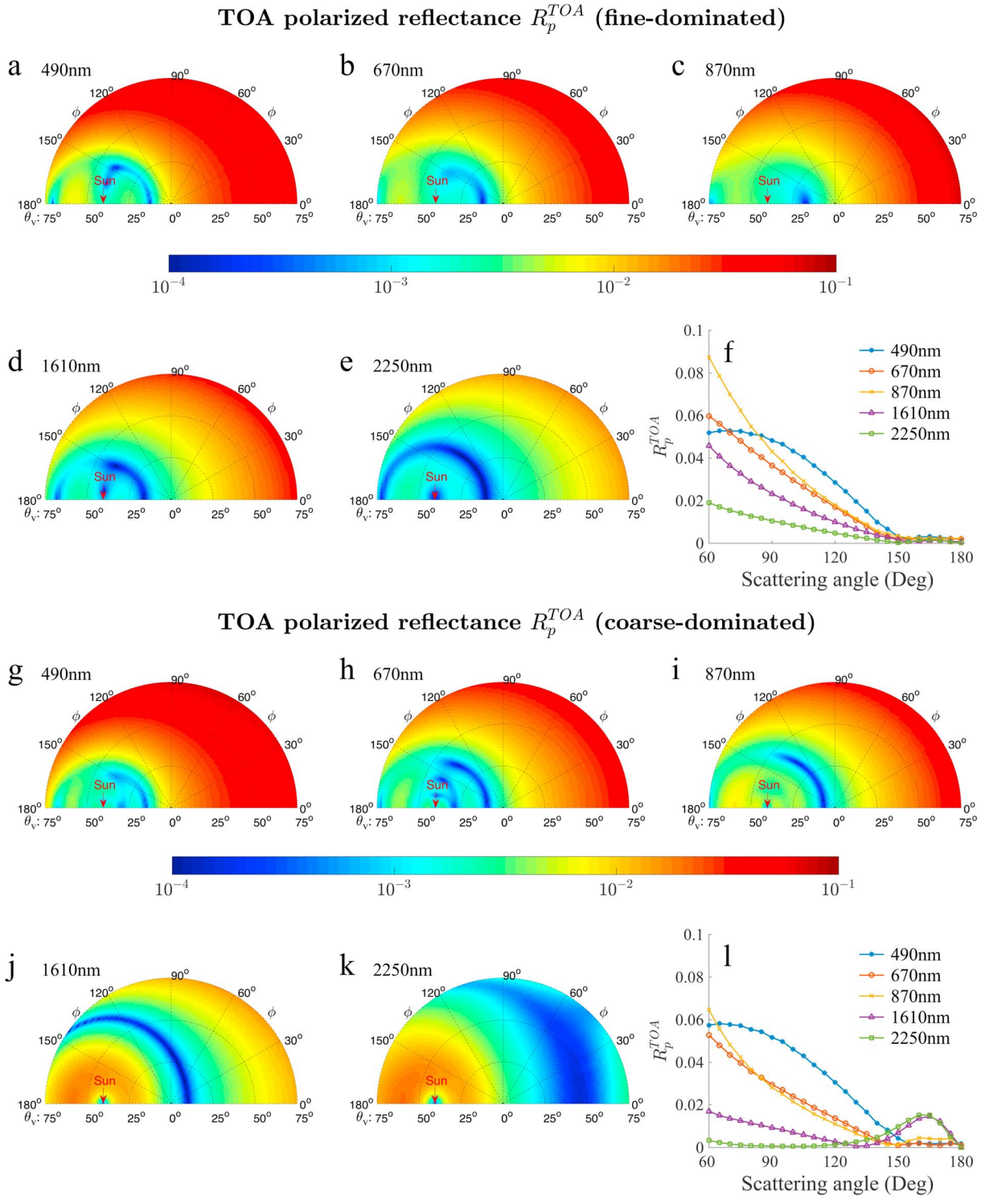

Figure 4. (a–e) The polar-plot of the TOA polarized reflectance R_p^{TOA} at 490, 670, 870, 1610, and 2250 nm using the same color bars for the fine-dominated case with an AOD of $\tau_a = 0.8$. (f) The mean R_p^{TOA} value (within an adjacent 5° range) as a function of the scattering ranging from 60° to 180° with a step of 5°. (g–l) Similar to Figures 4a–4f, but they are for the coarse-dominated case. The polar coordinates are defined similar to Figure 2.

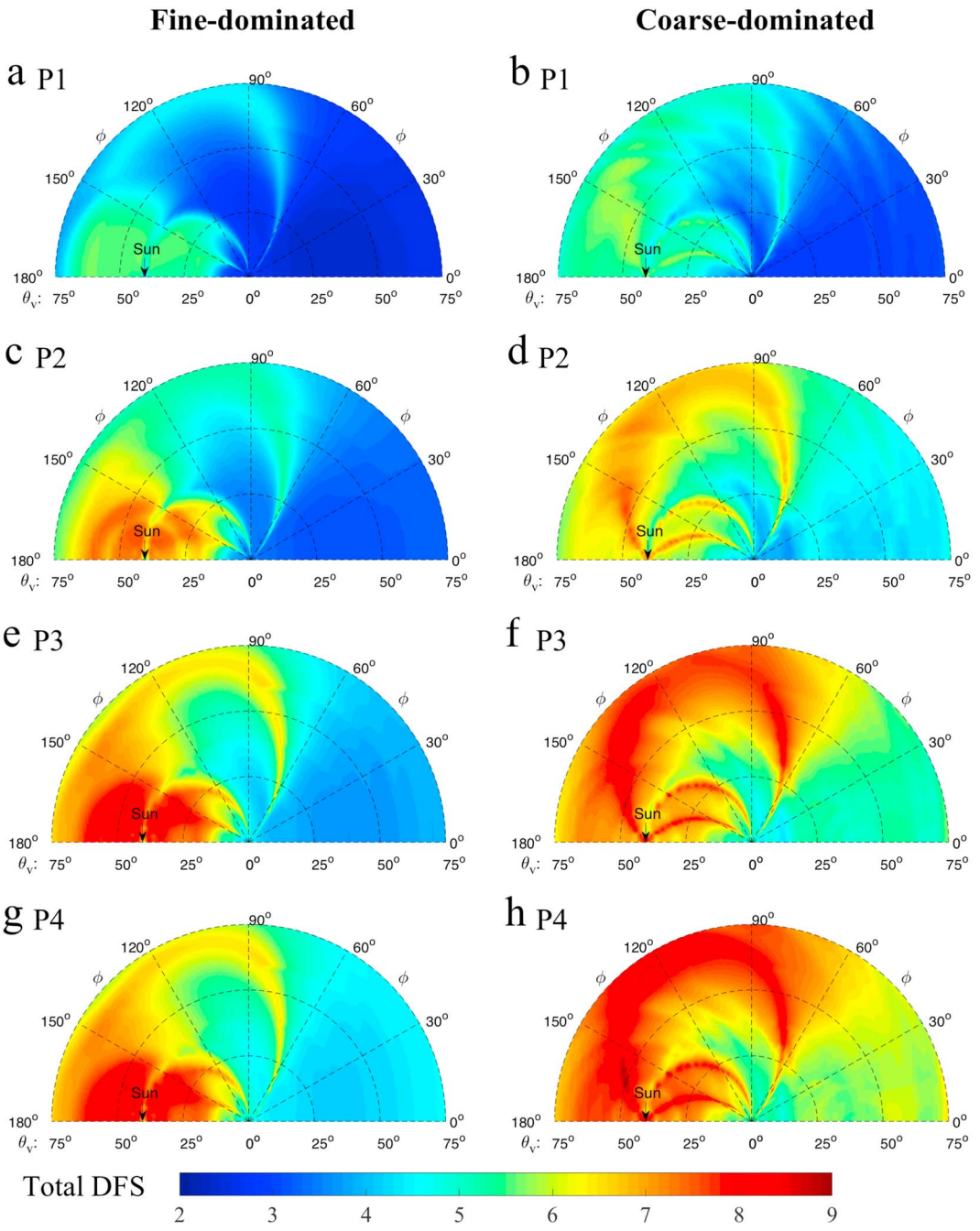

Figure 5. The polar plots of the total DFS with $\tau_a = 0.8$ for the different aerosol models in scenarios P1–P4. The left and right panels show the results for fine-dominated and coarse-dominated aerosols, respectively. The polar coordinates are defined similar to Figure 2.

dominated aerosols for the larger AOD case ($\tau_a = 0.8$). The total DFS ranges from 2 to 9 with the same color bar, and it depends upon the different observation scenarios, observation geometries, and aerosol models. The polar-plot results for the lower AOD case ($\tau_a = 0.2$), which are not shown here, demonstrate smaller values but similar angular distributions along the viewing geometries. To explain the angular distribution shown in Figure 5, Figure 6 further illustrates the mean total aerosol DFS (within an adjacent 10° range) as a function of the scattering angle ranging from 60° to 180° with a step of 10° for the four different observation scenarios, two aerosol models, and two AOD cases as well as the mean and standard

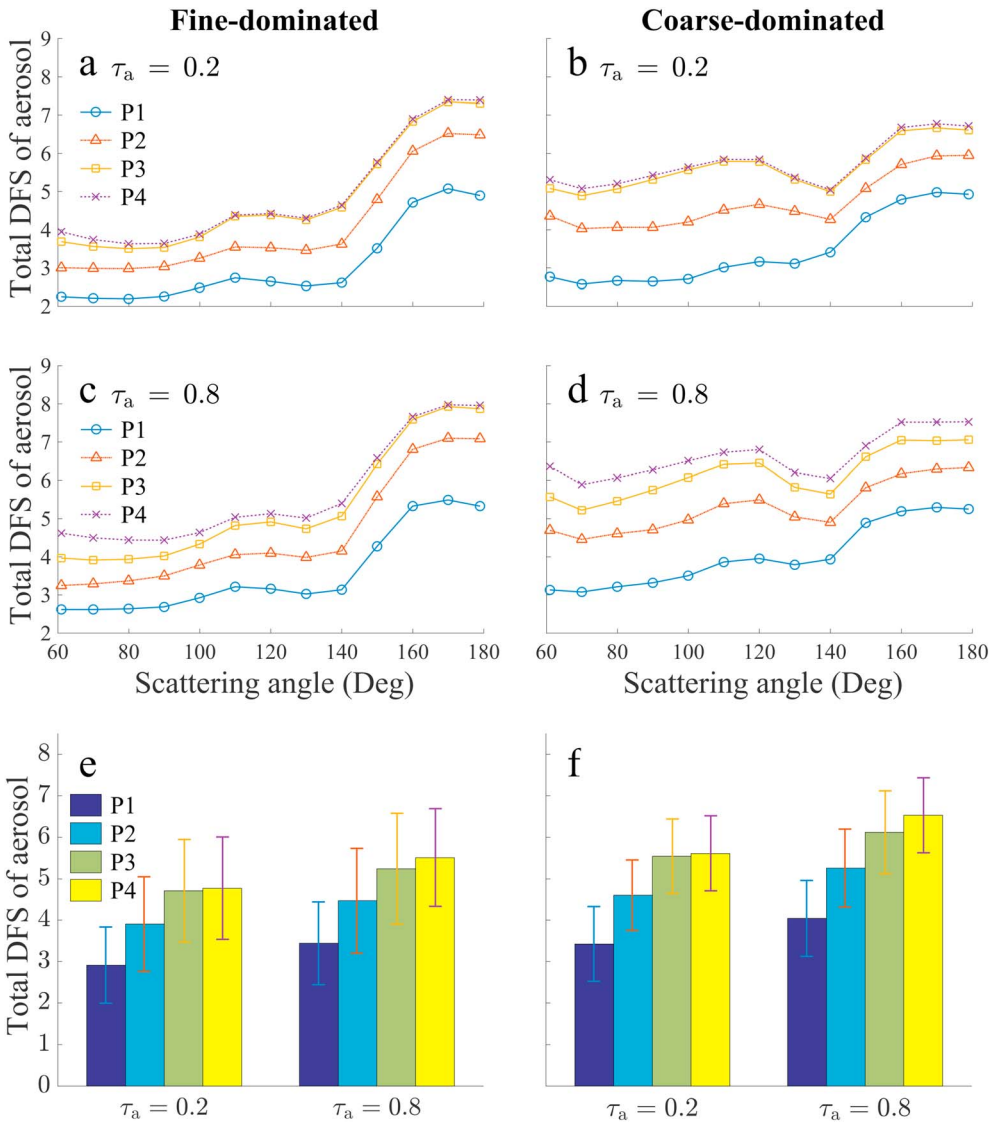

Figure 6. The mean total DFS of aerosols (within an adjacent 10° range) as a function of the scattering angle ranging from 60° to 180° with a step of 10° for each observations scenario (P1 through P4) as well as the mean and standard deviation of the total DFS presented in the format of a histogram with error bars using the statistics acquired for all of the considered observation geometries (θ_V = 0° – 75° and ϕ = 0° – 180°). The left and right panels show the results for the fine-dominated and coarse-dominated aerosols, respectively. (a–b) For the smaller and (c–d) larger AOD cases, respectively.

deviation of the total DFS along the hemispheric geometries (Θ = 60° – 180°) presented as a histogram with error bars.

From Figures 6a–6d, the total DFS values for the fine-dominated aerosols increase with an increase in the scattering angle ranging from 60° to 180° and sharply increase after Θ > 140° due to the contribution from coarse-mode aerosols to the information content, which will be further discussed later. Meanwhile, the total DFS values for the coarse-dominated aerosols also generally increase with an increase in the scattering angle ranging from 60° to 180°, but they exhibit a local minimum at approximately Θ = 140° in the range from 120° to 160° due to the influences of fine-mode aerosols, which will also be discussed in a later section. The mean total DFS values along the hemispheric geometries increase by at least 1 DFS after adding measurements of the polarized radiance at 1,610 and 2,250 nm, as shown in Figures 6e and 6f. In addition, by adding radiance measurements at 490 nm and 670 nm, the corresponding information content increases by approximately

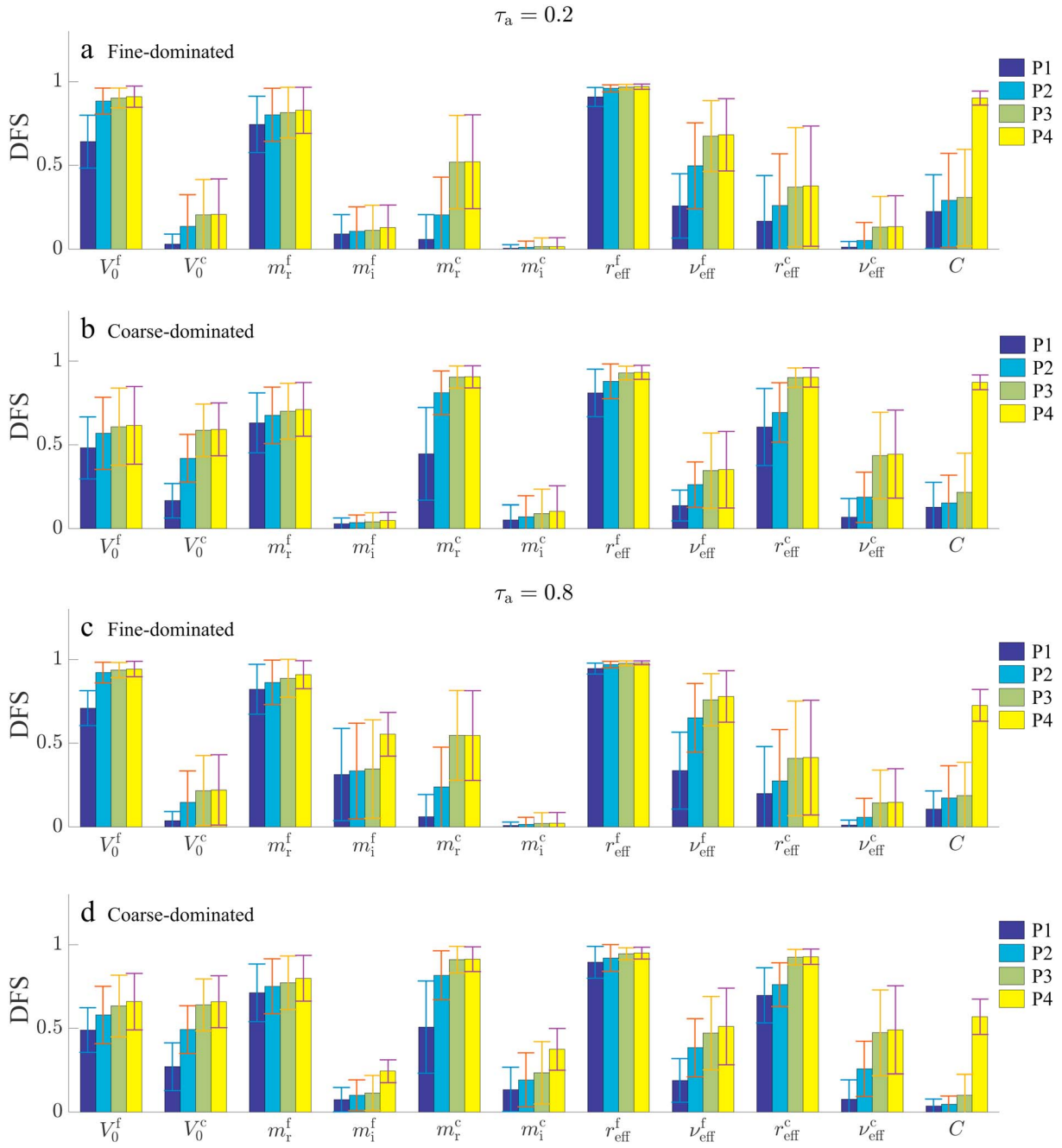

Figure 7. Same as Figures 6e–6f but for the DFS component of each aerosol parameter and one BPDF parameter. (a–b) For AODs of τ_a = 0.2 and (c–d) for τ_a = 0.8, respectively, for fine- and coarse-dominated aerosols.

0.1–0.5 DFS depending on the AOD and aerosol model. In addition, the larger AOD case (τ_a = 0.8) increases by approximately 0.5–1.0 DFS relative to the lower AOD case (τ_a = 0.2).

Based on this discussion on the total DFS of the aerosol retrieval, an increase of at least 2 DFS can be obtained by adding NIR measurements. Consequently, we have another question: how effective is a DFS increase of 2 at improving the ability to retrieve aerosol microphysical parameters? To answer this question, the DFS for each individual parameter is further analyzed in detail in the following subsection.

4.2. DFS of Each Retrieved Aerosol Parameter

To investigate the contribution from the information content to each retrieval parameter for the different scenarios, we investigate the information content for each parameter in the state vector in equation (18).

Figure 7 shows the mean and standard deviation of DFS for the simultaneous retrieval of the 10 aerosol parameters ($V_0^f, V_0^c, m_r^f, m_i^f, m_r^c, m_i^c, r_{eff}^f, v_{eff}^f, r_{eff}^c$, and v_{eff}^c) and one BPDF parameter (C) along the polar observation geometry ($\theta_v = 0° - 75°$ and $\phi = 0° - 180°$) as a histogram with error bars in consideration of two different AODs and two typical aerosol models.

Figure 7 clearly demonstrates that the insufficient information content from single-viewing measurements cannot support the simultaneous retrieval of 10 aerosol parameters with the BPDF parameter regardless of the magnitude of the AOD. However, for the smaller AOD case ($\tau_a = 0.2$), a few aerosol parameters could still be retrieved (DFS > 0.5) from the TOA measurements, and the DFS gradually approached saturation from scenario P1 to scenario P4. For example, three fine-mode parameters (e.g., V_0^f, m_r^f, and r_{eff}^f) could be retrieved for scenario P1 without the NIR measurements for fine-dominated aerosols, and one coarse-mode parameter (e.g., r_{eff}^c) together with two fine-mode parameters (e.g., m_r^f and r_{eff}^f) could be retrieved for coarse-dominated aerosols, albeit with relatively large uncertainties.

With an increase in the DFS of at least two from scenario P1 to scenario P4, one to three additional aerosol parameters could also be retrieved (DFS > 0.5) depending on the aerosol models and AOD. For example, when considering the larger AOD case ($\tau_a = 0.8$), an additional aerosol parameter (e.g., m_i^f) and the BPDF parameter (C) could be further retrieved for fine-dominated aerosols from scenario P1 to scenario P4, resulting in a DFS increase for m_r^f and C from 0.31 and 0.11 to 0.55 and 0.73, respectively. Amazingly, the imaginary part of the fine-mode refractive index (m_i^f) could be retrieved when adding two scalar radiance measurements to scenario P4, following which the mean DFS of m_i^f could be larger than 0.5. Consequently, to retrieve the fine-mode m_i^f in tandem with the other parameters for the larger AOD case, we must consider using radiance measurements in conjunction with polarization measurements, which is fundamentally consistent with previous work (Li et al., 2009). Meanwhile, three additional aerosol parameters (V_0^f, V_0^c, and m_r^c) and the BPDF parameter (C) could be further retrieved from scenario P1 to scenario P4 for coarse-dominated aerosols, following which the DFS values of V_0^f, V_0^f, m_r^c, and C could increase from 0.49, 0.26, 0.48, and 0.04 to 0.65, 0.66, 0.91, and 0.57, respectively.

Meanwhile, the changes in the DFS values of the aerosol parameters for the lower AOD case ($\tau_a = 0.2$) have trends similar to those for the larger AOD case from scenario P1 to scenario P4, except that the DFS values are smaller. In addition, the DFS value of C is larger than that for the larger AOD case; the DFS values reach 0.90 and 0.87 for fine- and coarse-dominated aerosols, respectively, when $\tau_a = 0.2$. Thus, we find that the BPDF parameter C is more easily retrieved in the lower AOD case than in the larger AOD case since the aerosols have a smaller influence on the surface at a lower AOD.

4.3. DFS Values and A Posteriori Errors of Selected Aerosol Parameters

Since these 10 aerosol parameters could not be simultaneously retrieved with the BPDF parameter because of the insufficient information content from single-viewing observations, then we consider predefining some parameters with a priori errors to constrain the retrievals of other, relatively important aerosol parameters such as the V_0^f, V_0^c, and m_i^f. Consequently, the fine-mode AOD, coarse-mode AOD, and absorption properties could be further derived. From the state vector elements in equations (23) and (25), we select six aerosol parameters ($V_0^f, V_0^c, m_r^f, m_i^f, r_{eff}^f$, and r_{eff}^c) for the retrieval of fine-dominated aerosols and six aerosol parameters ($V_0^f, V_0^c, m_r^c, m_i^c, r_{eff}^f$, and r_{eff}^c) for the retrieval of coarse-dominated aerosols.

Figure 8 illustrates the mean and standard deviation of the DFS values for the simultaneous retrieval of the six selected aerosol parameters with the BPDF parameter (C) for both the fine-dominated and the coarse-dominated aerosols, from which it is evident that the DFS of each selected parameter exhibits a significant improvement compared with these results shown in Figure 7. Corresponding to Figure 8, Figure 9 shows the mean and standard deviation of the a posteriori errors in the retrievals of the six selected aerosol parameters (corresponding to Figure 8) with the BPDF parameter; absolute errors are used for the complex refractive index parameters (i.e., m_r^f, m_i^f, m_r^c, and m_i^c), while relative errors are employed for the other parameters ($V_0^f, V_0^c, r_{eff}^f, r_{eff}^c$, and C). Here the a posteriori errors can be regarded as the theoretical retrieval errors of the retrieved parameters based on the a priori errors listed in Tables 2 and 3.

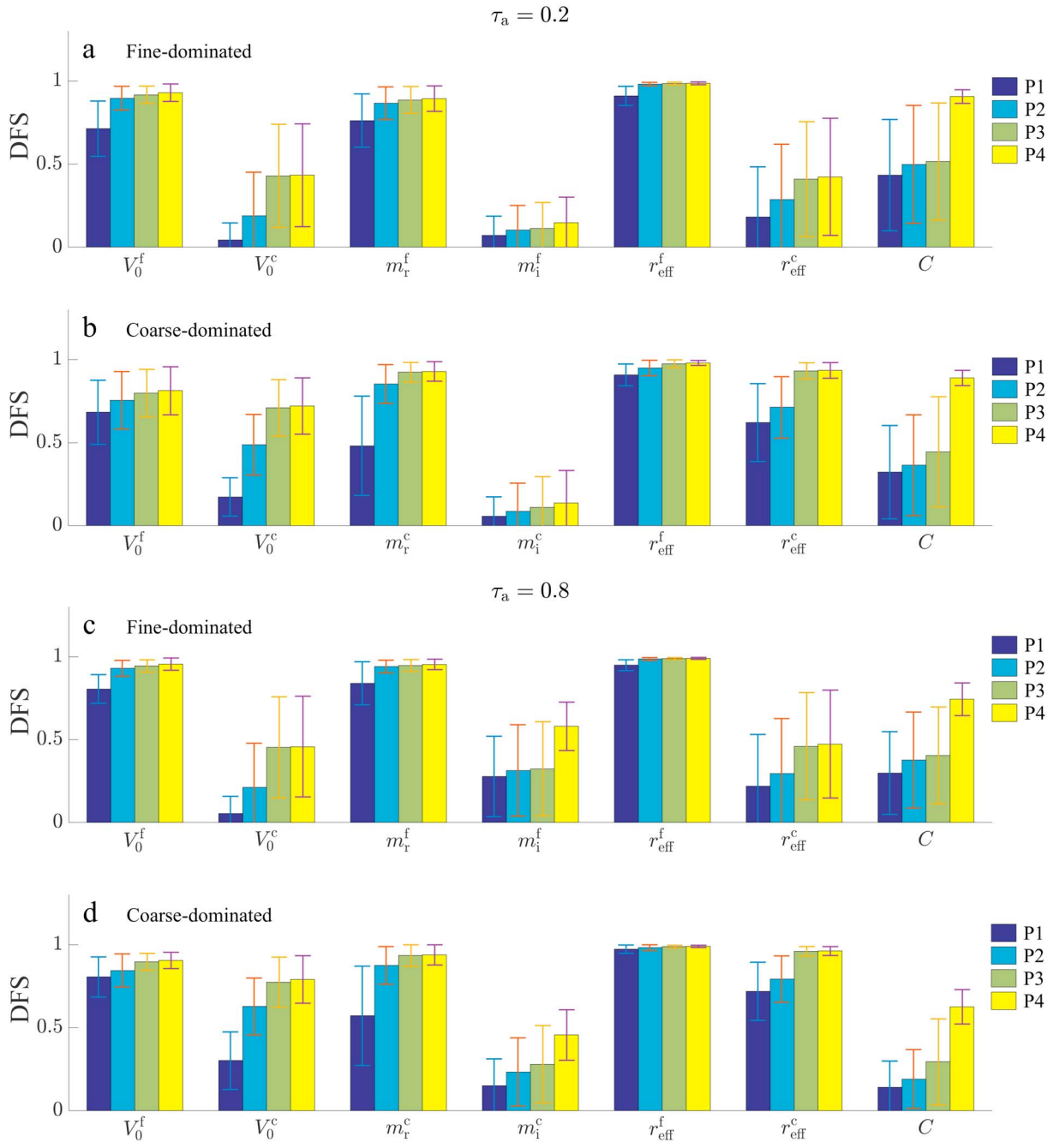

Figure 8. Same as Figure 7 but for six selected aerosol parameters and one BPDF parameter based on other predefined other aerosol parameters with a priori errors. The fine-mode m_r^f and m_i^f are selected for fine-dominated aerosols, while the coarse-mode m_r^c and m_i^c are selected for coarse-dominated aerosols.

From Figures 8 and 9, the fine-mode parameters V_0^f, m_r^f, and r_{eff}^f could be well retrieved for the fine-dominated aerosols by adding polarization measurements at 1,610 nm. For example, considering the larger AOD case, the DFS values of V_0^f, m_r^f, and r_{eff}^f increase from 0.80, 0.84, and 0.95 (scenario P1) to 0.93, 0.94, and 0.99 (scenario P2), and the retrieval errors decrease from 34%, 0.055 and 17% (scenario P1) to 20%, 0.035 and 8.8% (scenario P2), respectively. Subsequently, the DFS values and retrieval errors show little change with the adding of more measurements for scenarios P3 and P4. Even with a smaller AOD, these three fine-mode parameters could still be well effectively retrieved. In addition, when adding the scalar radiance measurements of two visible bands with their surface reflectance approximations estimated within the 2,250 nm

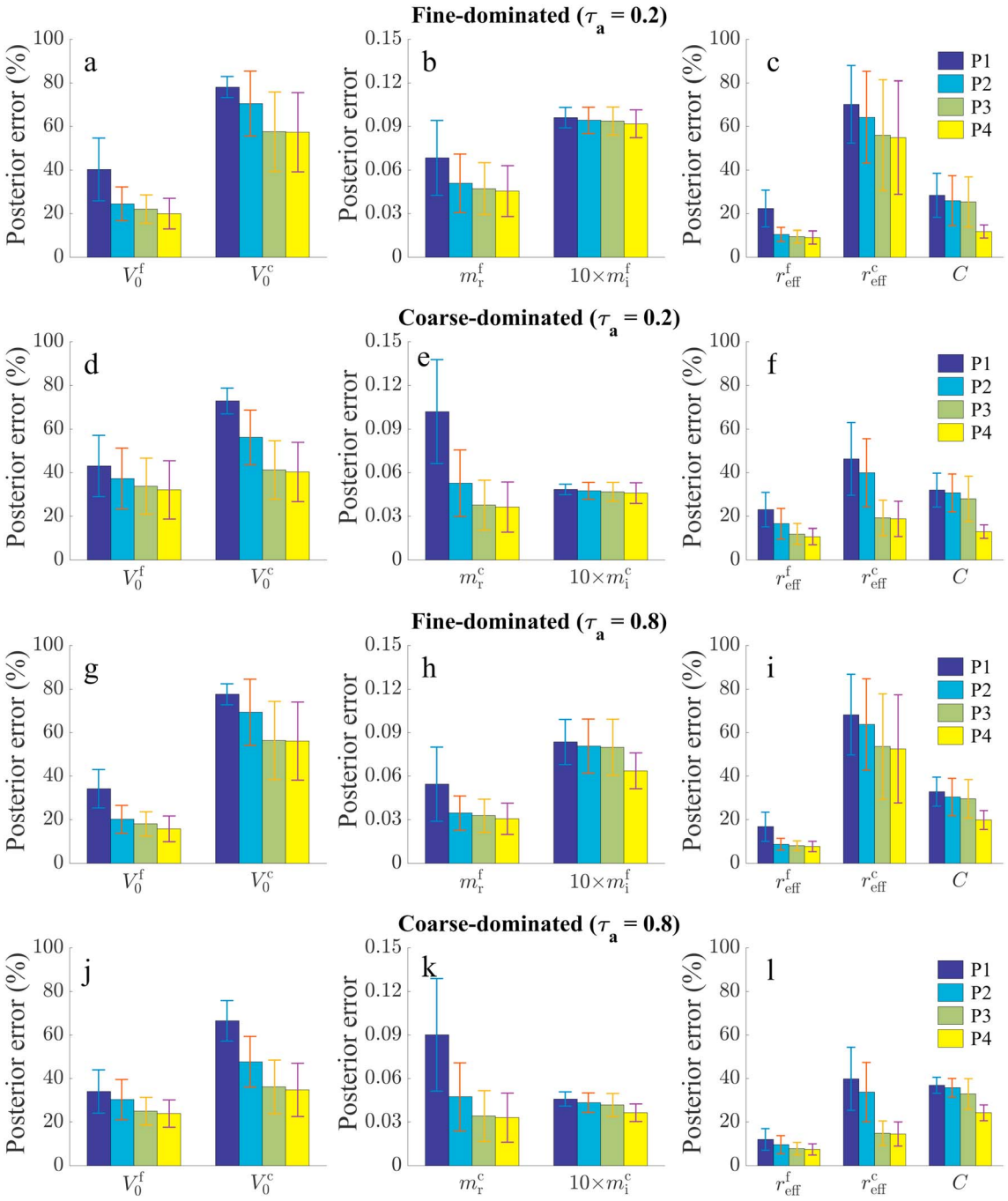

Figure 9. The mean and standard deviation of the posterior error in each of the six selected aerosol parameters and one BPDF parameter within the polar-observation geometry (θ_v = 0° – 75° and ϕ = 0° – 180°) for two different AODs and two different aerosol model cases. (a–f) For the AODs of τ_a = 0.2 and (g–l) for τ_a = 0.8, respectively, for the fine- and coarse-dominated aerosol model.

band, the fine-mode m_i^f could also be retrieved for the larger AOD case with an increase in the DFS from 0.32 (scenario P3) to 0.58 (scenario P4) and a decrease in the retrieval error (i.e., absolute error) from 0.008 (scenario P3) to 0.006 (scenario P4). Meanwhile, the BPDF parameter C could also be retrieved by adding the scalar radiance to the polarimetric measurements, because the scalar radiance contains more information than the polarization in the BPDF model based on the analysis results of the Jacobians discussed in Figure 2. Therefore, the inclusion of the scalar radiance in polarimetric measurements is

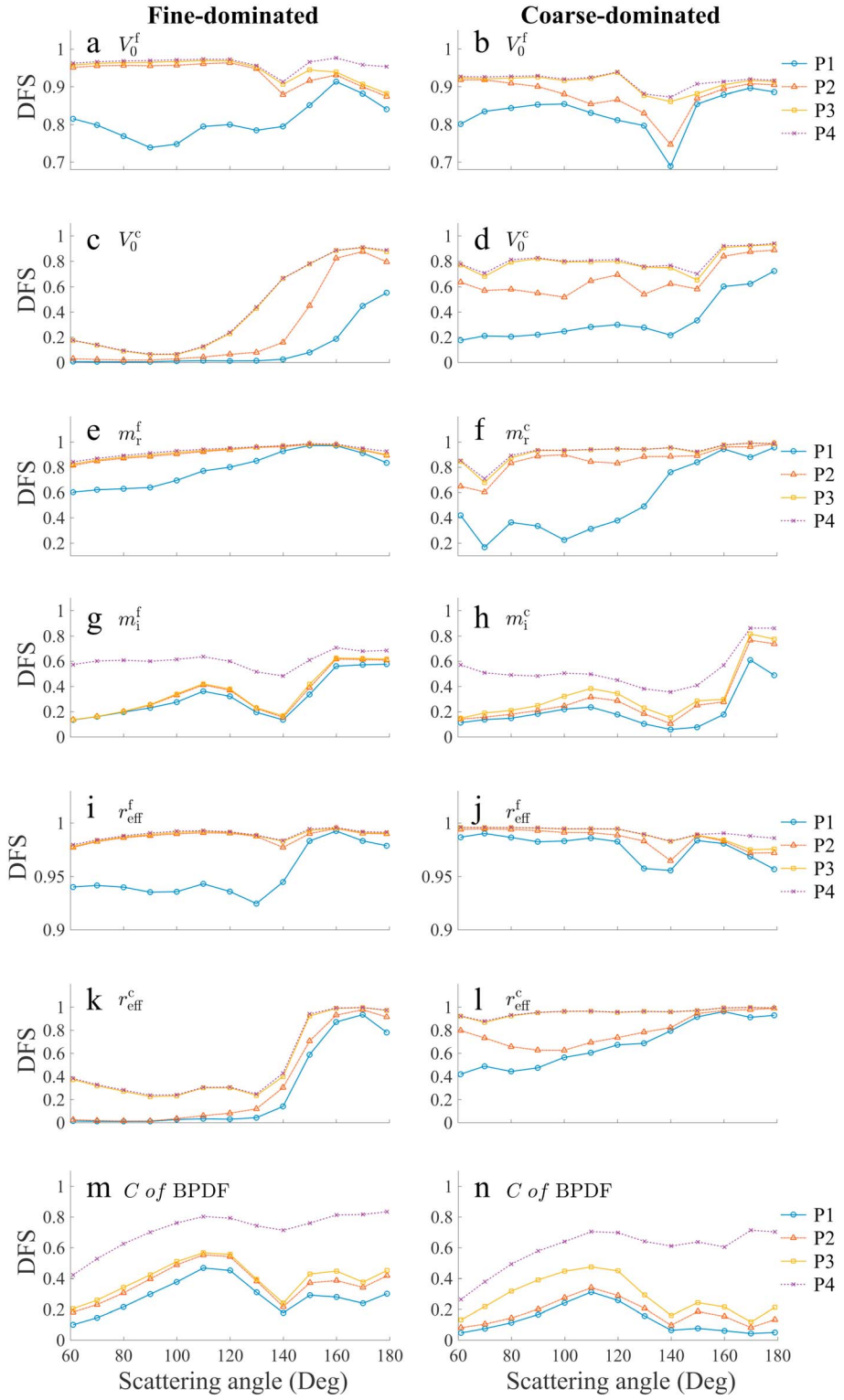

Figure 10. The mean DFS of each of the six selected aerosol parameters and the BPDF parameter (within an adjacent 10° range) as a function of the scattering angle ranging from 60° to 180° with a step of 10° for the larger AOD case (τ_a = 0.8). The left and right panels show the results for fine- and coarse-dominated aerosols, respectively. In addition, the fine-mode m_r^f and m_i^f are retrieved for fine-dominated aerosols, while the coarse-mode m_r^c and m_i^c are retrieved for coarse-dominated aerosols.

necessary for the retrieval of the BPDF parameter. In addition, the coarse-mode parameters V_0^c and r_{eff}^c are still difficult to retrieve because of their weak sensitivities characterized by DFS < 0.5 and a retrieval error of approximately 60% in most cases for both the smaller and the larger AOD cases.

Meanwhile, for the coarse-dominated aerosols, the fine-mode V_0^f and r_{eff}^f could be effectively retrieved with the coarse-mode V_0^c, m_r^c, and r_{eff}^c by adding the polarization measurement at 1,610 and 2,250 nm. Again, taking the larger AOD case, for example, the DFS value of V_0^f, V_0^c, m_r^c, r_{eff}^f, and r_{eff}^c could increase from 0.81, 0.30, 0.57, 0.97, and 0.72 (scenario P1) to 0.90, 0.77, 0.93, 0.99, and 0.96 (scenario P3), with decreases in the retrieval errors from 34%, 67%, 0.090, 12%, and 40% (scenario P1) to 25%, 37%, 0.034, 8%, and 15% (scenario P3), respectively. However, the coarse-mode m_i^c is difficult to retrieve with DFS < 0.5 due to the insufficient information content in most cases. The inclusion of the scalar radiance in polarimetric measurement is also indispensable for the retrieval of the BPDF parameter, since the DFS of C increases from 0.30 (scenario P3) to 0.63 (scenario P4) and the retrieval error decreases from 32% (scenario P3) to 24% (scenario P4).

Corresponding to Figures 8 and 9, Figures 10 and 11, respectively, reveal the mean DFS values and a posteriori errors for six selected aerosol parameters and the BPDF parameter (within an adjacent 10° range) as a function of the scattering angle ranging from 60° to 180° with a step of 10° for the larger AOD case. Accordingly, some detailed changes in the DFS values and retrieval errors along the scattering angle could be observed. For example, some of the coarse-mode parameters (e.g., V_0^c and r_{eff}^c) for the fine-dominated aerosols could be better retrieved in the range of $\Theta = 140° - 180°$ than in other scattering angles, which corresponds with the sharp increase in the total DFS for $\Theta > 140°$ as discussed in Figures 6a and 6c. Meanwhile, the DFS values of some aerosol parameters (e.g., V_0^f, V_0^c, m_r^c, and r_{eff}^c) for the coarse-dominated aerosols have a local minimum at approximately $\Theta = 140°$ in the range of $\Theta = 120° - 160°$ along the scattering angle, which mainly determines the trend of the total DFS as shown in Figures 6c and 6d.

4.4. Influences of Measurement Errors and Model Errors for Retrievals

To discuss the influences of measurement errors and model errors on the retrieval results, we analyze the posterior errors originating from various sources of observational noise and model errors, that is, the two terms of the observation covariance matrix in equation (8). The following analysis only focuses on scenario P4 for $\theta_0 = 40°$ and $\theta_v = 0°$ with nadir measurements ($\Theta = 140°$), because the DFS result from this observation geometry is representative of the mean and minimum of DFS values in all possible observation geometries for both fine-dominated and coarse-dominated aerosols. That is, if any parameter could be retrieved with this specific observation geometry, then that same parameter could also be retrieved at other observation geometries in most cases.

The DFS values and a posteriori errors for six selected aerosol parameters are plotted in Figure 12 as a function of the measurement errors for fine- and coarse-dominated aerosols for the larger AOD case under the assumption that the measurement error changes from 0.5% to 10% with a step of 0.5% and that the a priori errors do not changed. The DFS value of each parameter significantly decreases with an increase in the measurement error, and the retrieval error correspondingly increases with an increase in the measurement error. For example, with a change in the measurement error from 0.5% to 10%, the DFS values of V_0^f, m_r^f, and m_i^f for fine-dominated aerosols could decrease from 0.99, 0.99, and 0.72 to 0.95, 0.88, and 0.40, respectively, with increases in the retrieval errors from 10%, 0.017, and 0.006 to 18%, 0.052, and 0.008, respectively. If the measurement error is larger than 6%, then m_i^f will no longer be retrieved with DFS < 0.5. In addition, the DFS values of V_0^f, V_0^c, m_r^c, and r_{eff}^c for coarse-dominated aerosols could decrease from 0.97, 0.92, 0.98, and 0.97 to 0.86, 0.70, 0.87, and 0.86, respectively, with increases in the retrieval errors increasing from 13%, 22%, 0.019, and 13% to 30%, 44%, 0.051, and 30%, respectively.

Figure 13 illustrates the DFS values and a posteriori errors for six selected aerosol parameters as a function of the model errors in the fine- and coarse-dominated aerosols for the larger AOD case. These six variables are not selected for retrieval, but they can significantly affect the radiative quantity. The model error corresponds with the combination of three predefined aerosol parameters, namely, $\{m_i^c, v_{eff}^f, v_{eff}^c\}$ for fine-dominated aerosols and $\{m_i^f, v_{eff}^f, v_{eff}^c\}$ for coarse-dominated aerosols, which change from 5% to 80% with a step of 5%. Meanwhile, the a priori errors in the other parameters do not change, and the measurement error is 5%, which are the same settings as those in sections 4.1–4.3. In contrast with the measurement error case,

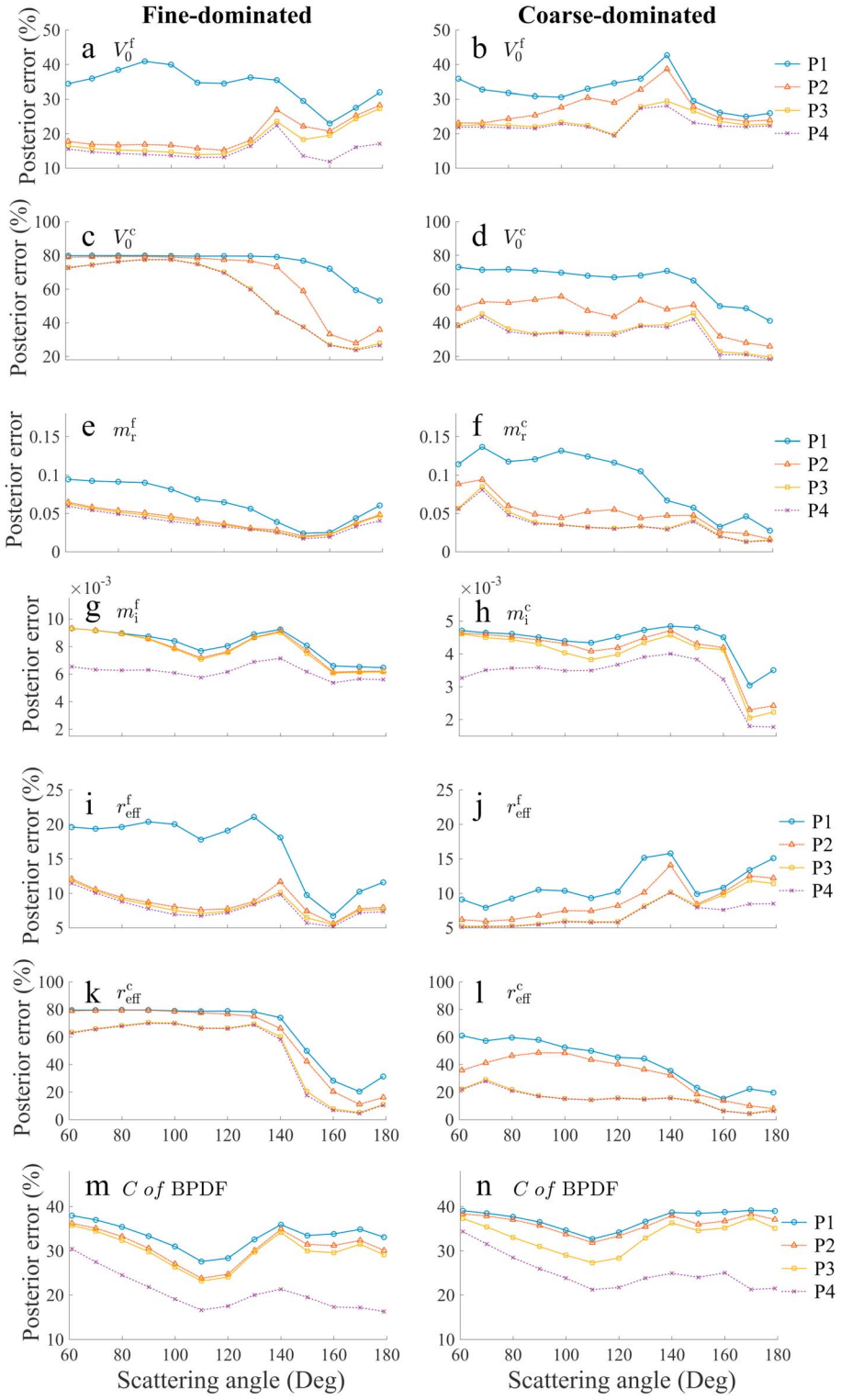

Figure 11. Same as Figure 10 but for the posterior error results. (e–h) The absolute errors are used for the parameters of complex refractive indices (m_r^f, m_r^c, m_i^f, and m_i^c), while the relative errors are used for the other parameters.

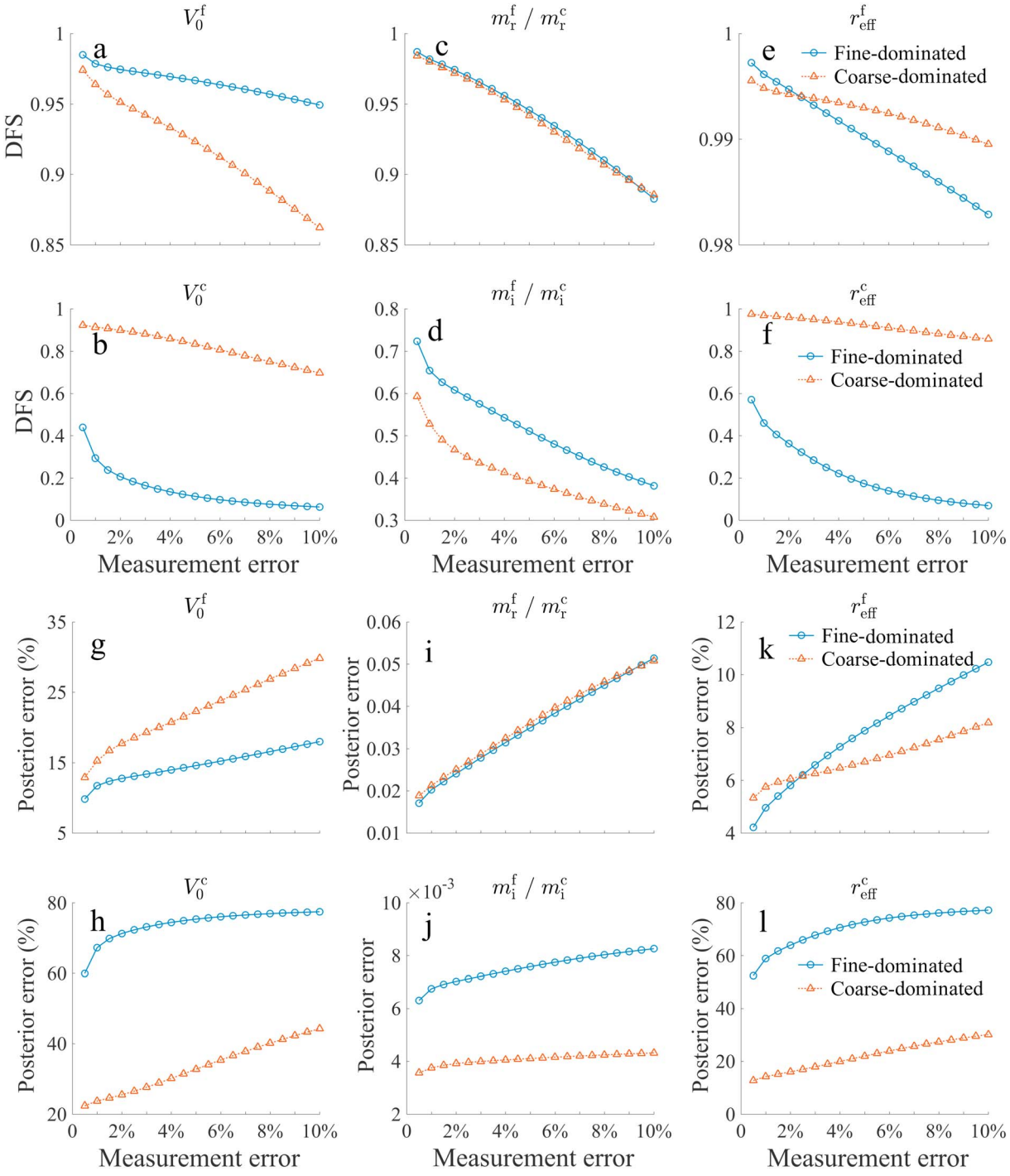

Figure 12. The DFS and a posteriori error for each of the six selected aerosol parameters as a function of the measurement errors in the fine- and coarse-dominated aerosols, respectively, for scenario P4 under the assumption that the measurement error changes from 0.5% to 10% with a step of 0.5% and that the a priori errors do not change. The simulations are performed with an observation geometry of $\theta_0 = 40°$ and $\theta_v = 0°$ ($\Theta = 140°$) for the larger AOD case ($\tau_a = 0.8$). In addition, the fine-mode m_r^f and m_i^f are selected for fine-dominated aerosols, while the coarse-mode m_r^c and m_i^c are selected for coarse-dominated aerosols.

the model error has a relatively small effect on the retrieval uncertainties for these selected parameters. From Figure 13, with the exception of two fine-mode parameters (m_r^f and r_{eff}^f) for fine-dominated aerosols and two coarse-mode parameters (V_0^c and m_r^c) for coarse-dominated aerosols, it is apparent that the uncertainties in the other parameters impose few changes with the model errors ranging from 5% to 80%.

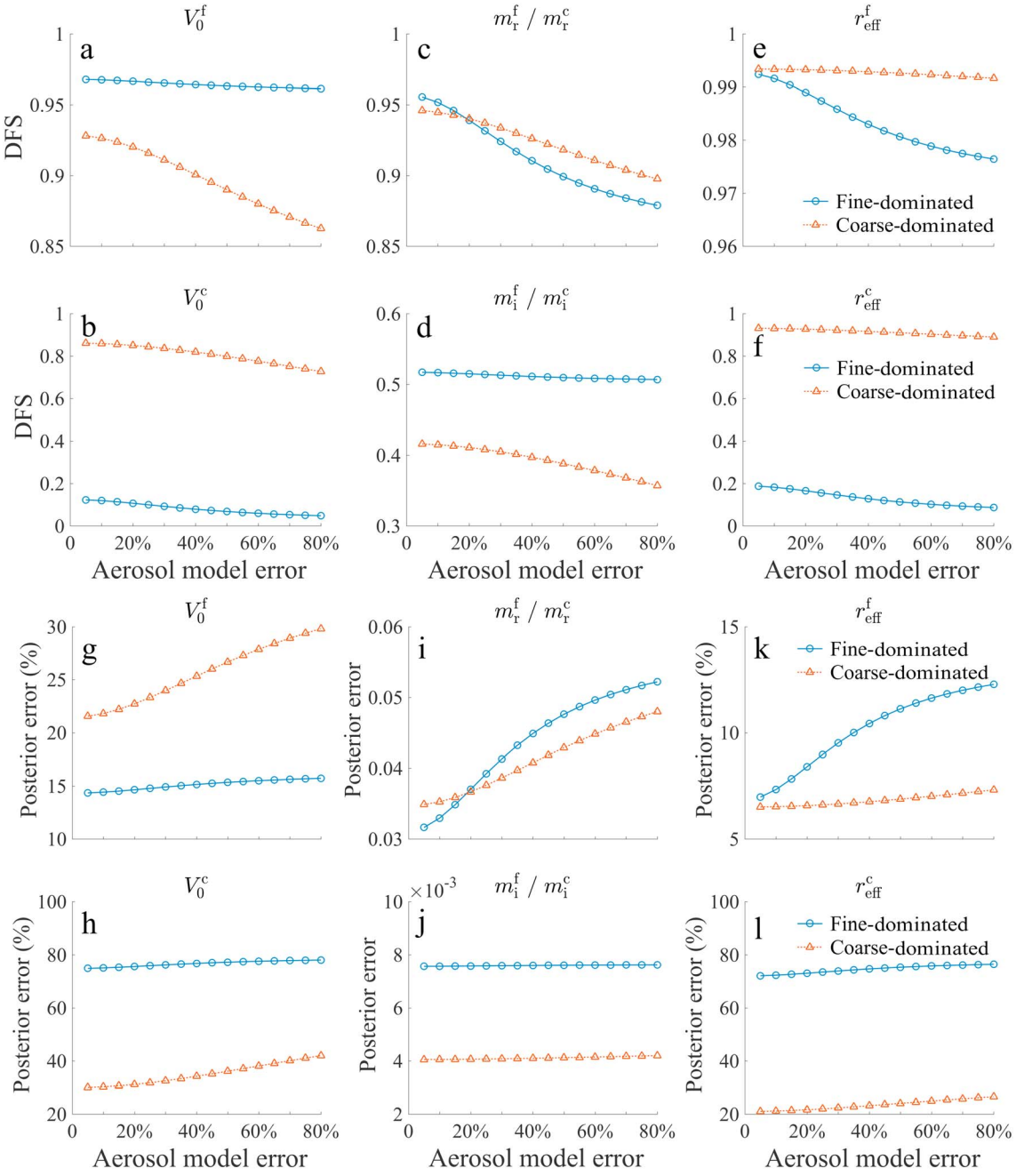

Figure 13. Same as Figure 12 but for model errors ranging from 5% to 80% with a step of 5%. Meanwhile, the a priori errors in the other parameters and the measurement errors do not change.

5. Summary and Conclusions

Following the synthetic data simulated using UNL-VTM from multispectral single-viewing polarization and radiance measurements over vegetated land for various scenarios, we conduct an information content and retrieval error analysis for aerosol microphysical properties through the inclusion of NIR polarimetric measurements. Our findings can be summarized into several conclusions as follows.

1. For fine-dominated aerosols, at least three fine-mode aerosol parameters (e.g., V_0^f, m_r^f, and r_{eff}^f) could be simultaneously well retrieved by adding NIR measurements. In addition, the fine-mode m_i^f can also be retrieved with the radiance and polarization for the larger AOD case (τ_a = 0.8). However, the coarse-

mode parameters could not be retrieved due to their weak sensitivities, even for the larger AOD cases (τ_a = 0.8). Meanwhile, for the coarse-dominated aerosols, two fine-mode parameters (V_0^f and r_{eff}^f) and three fine-mode parameters (V_0^c, m_r^c, and r_{eff}^c) could be simultaneously retrieved by adding NIR measurements.

2. If only TOA polarization data at shorter wavelengths (490, 670, and 870 nm) are used without NIR measurements (scenario P1), the fine-mode parameters V_0^f, m_r^f, and r_{eff}^f can also be retrieved for the fine-dominated aerosols, albeit with a significantly larger retrieval uncertainty than obtained during the other three scenarios that incorporate NIR measurements. For example, considering the larger AOD case (τ_a = 0.8), the posterior errors in V_0^f, m_r^f, and r_{eff}^f could decrease from 34%, 0.055, and 17% in scenario P1 to 20%, 0.035, and 8.8% in scenario P2, respectively. In addition, those retrieval errors demonstrate only negligible changes with the addition of more measurements for scenarios P3 and P4. Therefore, the 1,610 nm band is necessary for the effective retrieval of the fine-mode V_0^f, m_r^f, and r_{eff}^f parameters in combination with shorter-wavelength bands for fine-dominated aerosols.
3. For coarse-dominated aerosols, the coarse-mode V_0^c (and hence the coarse-mode AOD) cannot be retrieved together with V_0^f because of an insufficient information content due to the absence of NIR polarimetric measurements. By adding polarization measurements at 1,610 and 2,250 nm, the retrieval uncertainties in V_0^f, V_0^c, m_r^c, r_{eff}^f, and r_{eff}^c could decrease from 34%, 67%, 0.090, 12%, and 40% in scenario P1 to 25%, 37%, 0.034, 8%, and 15% in scenario P3, respectively, for the larger AOD case (τ_a = 0.8). Thus, the 1,610 and 2,250 nm bands are both indispensable for the more effective retrieval of coarse-dominated parameters, especially V_0^c. In addition, if polarization measurements at 2,250 nm are not included, the coarse-mode parameter V_0^c cannot be retrieved for the smaller AOD case.
4. The analysis results for the DFS values and retrieval errors also show that the scalar radiance contains more useful information than the polarization in the BPDF model and that the BPDF parameter *C* could be further retrieved in tandem with the aerosol parameters by including the scalar radiance in polarimetric measurements. Therefore, when only the polarization is used for the aerosol retrieval, the BPDF parameter *C* should be prescribed.
5. Measurement errors have significantly larger influences on the retrieval uncertainties than the assumptions associated with the model parameters, and the posterior errors in the retrieved aerosol parameters correspondingly increase with an increase in the measurement errors and model errors.

The findings in this study constitute important guidance for the development of algorithms for the retrieval of aerosol microphysical properties from multispectral polarimetric measurements at NIR wavelength bands, such as those acquired using the spaceborne PSAC instrument. We focus on an information content analysis over vegetated land, and thus, the surface could be approximately estimated at two visible wavelengths (490 and 670 nm) using the TOA measurements at 2,250 nm. In a future study, we will consider introducing the theoretical framework developed for the hyperspectral remote sensing of aerosols (Hou et al., 2016, 2017) to take full advantage of the all available multispectral measurements to retrieve the aerosol parameters for various surface types including bright urban surfaces.

Acknowledgments
This study was supported by the National Natural Science Foundation of China (grant 41505022, 41671367, and 41601383), the Open Fund of State Key Laboratory of Remote Sensing Science (grant OFSLRSS201710), and the Instrument Developing Project of the Chinese Academy of Sciences (grant YZ201664). We also acknowledge the Holland Computing Center (HCC) at the University of Nebraska-Lincoln and the High Performance Computing (HPC) System at The University of Iowa for their computational support. The data and Fortran codes used for the forward simulations and the information content analysis are available at the link in the UNL-VRTM website (www.unl-vrtm.com).

References

Breon, F.-M., & Maignan, F. (2017). A BRDF–BPDF database for the analysis of Earth target reflectances. *Earth System Science Data*, *9*(1), 31–45. https://doi.org/10.5194/essd-9-31-2017

Byrd, R., Lu, P., Nocedal, J., & Zhu, C. (1995). A limited memory algorithm for bound constrained optimization. *SIAM Journal on Scientific Computing*, *16*(5), 1190–1208. https://doi.org/10.1137/0916069

Chen, J., & Cihlar, J. (1997). A hotspot function in a simple bidirectional reflectance model for satellite applications. *Journal of Geophysical Research*, *102*(D22), 25,907–25,913. https://doi.org/10.1029/97JD02010

Chen, X., Wang, J., Liu, Y., Xu, X., Cai, Z., Yang, D., et al. (2017). Angular dependence of aerosol information content in CAPI/TanSat observation over land: Effect of polarization and synergy with A-train satellites. *Remote Sensing of Environment*, *196*, 163–177. https://doi.org/10.1016/j.rse.2017.05.007

Chen, X., Yang, D., Cai, Z., Liu, Y., & Spurr, R. (2017). Aerosol retrieval sensitivity and error analysis for the cloud and aerosol polarimetric imager on board TanSat: The effect of multi-angle measurement. *Remote Sensing*, *9*(3), 183. https://doi.org/10.3390/rs9020183

Chowdhary, J., Cairns, B., Mishchenko, M., & Travis, L. (2001). Retrieval of aerosol properties over the ocean using multispectral and multiangle photopolarimetric measurements from the Research Scanning Polarimeter. *Geophysical Research Letters*, *28*(2), 243–246. https://doi.org/10.1029/2000GL011783

Corradini, S., & Cervino, M. (2006). Aerosol extinction coefficient profile retrieval in the oxygen A-band considering multiple scattering atmosphere. Test case: SCIAMACHY nadir simulated measurements. *Journal of Quantitative Spectroscopy and Radiation*, *97*(3), 354–380. https://doi.org/10.1016/j.jqsrt.2005.05.061

Deuzé, J. L., Goloub, P., Herman, M., Marchand, A., Perry, G., Susana, S., & Tanré, D. (2000). Estimate of the aerosol properties over the ocean with POLDER. *Journal of Geophysical Research*, *105*(D12), 15,329–15,346. https://doi.org/10.1029/2000JD900148

Deuzé, J. L., Bréon, F. M., Devaux, C., Goloub, P., Herman, M., Lafrance, B., et al. (2001). Remote sensing of aerosols over land surfaces from POLDER-ADEOS-1 polarized measurements. *Journal of Geophysical Research*, *106*(D5), 4913–4926. https://doi.org/10.1029/2000JD900364

Diner, D. J., Beckert, J. C., Reilly, T. H., Bruegge, C. J., Conel, J. E., Kahn, R. A., et al. (1998). Multi-angle Imaging SpectroRadiometer (MISR) instrument description and experiment overview. *IEEE Transactions on Geoscience and Remote*, *36*(4), 1072–1087. https://doi.org/10.1109/36.700992

Ding, S., Wang, J., & Xu, X. (2016). Polarimetric remote sensing in oxygen A and B bands: Sensitivity study and information content analysis for vertical profile of aerosols. *Atmospheric Measurement Techniques*, *9*(5), 2077–2092. https://doi.org/10.5194/amt-9-2077-2016

Drury, E., Jacob, D. J., Spurr, R. J. D., Wang, J., Shinozuka, Y., Anderson, B. E., et al. (2010). Synthesis of satellite (MODIS), aircraft (ICARTT), and surface (IMPROVE, EPA-AQS, AERONET) aerosol observations over eastern North America to improve MODIS aerosol retrievals and constrain surface aerosol concentrations and sources. *Journal of Geophysical Research*, *115*, D14204. https://doi.org/10.1029/2009JD012629

Dubovik, O., & King, M. D. (2000). A flexible inversion algorithm for retrieval of aerosol optical properties from Sun and sky radiance measurements. *Journal of Geophysical Research*, *105*(D16), 20,673–20,696. https://doi.org/10.1029/2000JD900282

Dubovik, O., Smirnov, A., Holben, B. N., King, M. D., Kaufman, Y. J., Eck, T. F., & Slutsker, I. (2000). Accuracy assessments of aerosol optical properties retrieved from Aerosol Robotic Network (AERONET) Sun and sky radiance measurements. *Journal of Geophysical Research*, *105*(D8), 9791–9806. https://doi.org/10.1029/2000JD900040

Dubovik, O., Herman, M., Holdak, A., Lapyonok, T., Tanré, D., Deuzé, J. L., et al. (2011). Statistically optimized inversion algorithm for enhanced retrieval of aerosol properties from spectral multi-angle polarimetric satellite observations. *Atmospheric Measurement Techniques*, *4*(5), 975–1018. https://doi.org/10.5194/amt-4-975-2011

Dubovik, O., Lapyonok, T., Litvinov, P., Herman, M., Fuertes, D., Ducos, F., et al. (2014). GRASP: A versatile algorithm for characterizing the atmosphere. *SPIE Newsroom*. https://doi.org/10.1117/2.1201408.005558

Frankenberg, C., Hasekamp, O., O'Dell, C., Sanghavi, S., Butz, A., & Worden, J. (2012). Aerosol information content analysis of multi-angle high spectral resolution measurements and its benefit for high accuracy greenhouse gas retrievals. *Atmospheric Measurement Techniques*, *5*(7), 1809–1821. https://doi.org/10.5194/amt-5-1809-2012

Gatebe, C. K., & King, M. D. (2016). Airborne spectral BRDF of various surface types (ocean, vegetation, snow, desert, wetlands, cloud decks, smoke layers) for remote sensing applications. *Remote Sensing of Environment*, *179*, 131–148. https://doi.org/10.1016/j.rse.2016.03.029

Goloub, P., Waquet, F., Deuze, J. L., Herman, M., Auriol, F., Leon, J. F., et al. (2003). *Development of a multispectral polarimeter dedicated to aerosol characterization – preliminary results*. Paper presented at IGARSS 2003. 2003 IEEE International Geoscience and Remote Sensing Symposium. Proceedings (IEEE Cat. No. 03CH37477), 21–25 July 2003.

Han, C., Wang, Y., & He, G. (2009). On the convergence of asynchronous parallel algorithm for large-scale linearly constrained minimization problem. *Applied Mathematics and Computation*, *211*(2), 434–441. https://doi.org/10.1016/j.amc.2009.01.081

Hasekamp, O. P., & Landgraf, J. (2005a). Linearization of vector radiative transfer with respect to aerosol properties and its use in satellite remote sensing. *Journal of Geophysical Research*, *110*, D04203. https://doi.org/10.1029/2004JD005260

Hasekamp, O. P., & Landgraf, J. (2005b). Retrieval of aerosol properties over the ocean from multispectral single-viewing-angle measurements of intensity and polarization: Retrieval approach, information content, and sensitivity study. *Journal of Geophysical Research*, *110*, D20207. https://doi.org/10.1029/2005JD006212

Herman, M., Deuzé, J. L., Devaux, C., Goloub, P., Bréon, F. M., & Tanré, D. (1997). Remote sensing of aerosols over land surfaces including polarization measurements and application to POLDER measurements. *Journal of Geophysical Research*, *102*(D14), 17,039–17,049. https://doi.org/10.1029/96JD02109

Hess, M., Koepke, P., & Schult, I. (1998). Optical properties of aerosols and clouds: The software package OPAC. *Bulletin of the American Meteorological Society*, *79*(5), 831–844. https://doi.org/10.1175/1520-0477(1998)079%3C0831:OPOAAC%3E2.0.CO;2

Holben, B. N., Eck, T. F., Slutsker, I., Tanré, D., Buis, J. P., Setzer, A., et al. (1998). AERONET—A federated instrument network and data archive for aerosol characterization. *Remote Sensing of Environment*, *66*(1), 1–16. https://doi.org/10.1016/S0034-4257(98)00031-5

Holben, B. N., Tanré, D., Smirnov, A., Eck, T. F., Slutsker, I., Abuhassan, N., et al. (2001). An emerging ground-based aerosol climatology: Aerosol optical depth from AERONET. *Journal of Geophysical Research*, *106*(D11), 12,067–12,097. https://doi.org/10.1029/2001JD900014

Holzer-Popp, T., Schroedter-Homscheidt, M., Breitkreuz, H., Martynenko, D., & Klüser, L. (2008). Improvements of synergetic aerosol retrieval for ENVISAT. *Atmospheric Chemistry and Physics*, *8*(24), 7651–7672. https://doi.org/10.5194/acp-8-7651-2008

Hou, W., Qie, L., Li, Z., Sun, X., Hong, J., Chen, X., et al. (2015). Study on pixel matching method of the multi-angle observation from airborne AMPR measurements, paper presented at Applied Optics and Photonics China (AOPC2015). *Proceedings of SPIE*, *9675*, 96751Z-1-6. https://doi.org/10.1117/12.2199777

Hou, W., Wang, J., Xu, X., Reid, J. S., & Han, D. (2016). An algorithm for hyperspectral remote sensing of aerosols: 1. Development of theoretical framework. *Journal of Quantitative Spectroscopy and Radiation*, *178*, 400–415. https://doi.org/10.1016/j.jqsrt.2016.01.019

Hou, W., Wang, J., Xu, X., & Reid, J. S. (2017). An algorithm for hyperspectral remote sensing of aerosols: 2. Information content analysis for aerosol parameters and principal components of surface spectra. *Journal of Quantitative Spectroscopy and Radiation*, *192*, 14–29. https://doi.org/10.1016/j.jqsrt.2017.01.041

Hsu, N. C., Si-Chee, T., King, M. D., & Herman, J. R. (2004). Aerosol properties over bright-reflecting source regions. *IEEE Transactions on Geoscience and Remote*, *42*(3), 557–569. https://doi.org/10.1109/TGRS.2004.824067

Hsu, N. C., Si-Chee, T., King, M. D., & Herman, J. R. (2006). Deep Blue retrievals of Asian aerosol properties during ACE-Asia. *IEEE Transactions on Geoscience and Remote*, *44*(11), 3180–3195. https://doi.org/10.1109/TGRS.2006.879540

Jeong, U., Kim, J., Ahn, C., Torres, O., Liu, X., Bhartia, P. K., et al. (2016). An optimal-estimation-based aerosol retrieval algorithm using OMI near-UV observations. *Atmospheric Chemistry and Physics*, *16*(1), 177–193. https://doi.org/10.5194/acp-16-177-2016

Kahn, R. A., Gaitley, B. J., Martonchik, J. V., Diner, D. J., Crean, K. A., & Holben, B. (2005). Multiangle Imaging Spectroradiometer (MISR) global aerosol optical depth validation based on 2 years of coincident Aerosol Robotic Network (AERONET) observations. *Journal of Geophysical Research*, *110*, D10S04. https://doi.org/10.1029/2004JD004706

Kaufman, Y. J., Tanré, D., Remer, L. A., Vermote, E. F., Chu, A., & Holben, B. N. (1997). Operational remote sensing of tropospheric aerosol over land from EOS moderate resolution imaging spectroradiometer. *Journal of Geophysical Research*, *102*(D14), 17,051–17,067. https://doi.org/10.1029/96JD03988

Kaufman, Y. J., Wald, A. E., Remer, L. A., Gao, B.-C., Li, R.-R., & Flynn, L. (1997). The MODIS 2.1-μm channel-correlation with visible reflectance for use in remote sensing of aerosol. *IEEE Transactions on Geoscience and Remote*, *35*(5), 1286–1298.

Kaufman, Y. J., Tanre, D., & Boucher, O. (2002). A satellite view of aerosols in the climate system. *Nature*, *419*(6903), 215–223. https://doi.org/10.1038/nature01091

King, M. D., Kaufman, Y. J., Tanré, D., & Nakajima, T. (1999). Remote sensing of tropospheric aerosols from space: Past, present, and future. *Bulletin of the American Meteorological Society*, *80*(11), 2229–2259. https://doi.org/10.1175/1520-0477(1999)080%3C2229:RSOTAF%3E2.0.CO;2

Kleidman, R. G., O'Neill, N. T., Remer, L. A., Kaufman, Y. J., Eck, T. F., Tanré, D., et al. (2005). Comparison of Moderate Resolution Imaging Spectroradiometer (MODIS) and Aerosol Robotic Network (AERONET) remote-sensing retrievals of aerosol fine mode fraction over ocean. *Journal of Geophysical Research*, *110*, D22205. https://doi.org/10.1029/2005JD005760

Knobelspiesse, K., Cairns, B., Redemann, J., Bergstrom, R. W., & Stohl, A. (2011). Simultaneous retrieval of aerosol and cloud properties during the MILAGRO field campaign. *Atmospheric Chemistry and Physics*, *11*(13), 6245–6263. https://doi.org/10.5194/acp-11-6245-2011

Knobelspiesse, K., Cairns, B., Mishchenko, M., Chowdhary, J., Tsigaridis, K., van Diedenhoven, B., et al. (2012). Analysis of fine-mode aerosol retrieval capabilities by different passive remote sensing instrument designs. *Optics Express*, *20*(19), 21457–21484. https://doi.org/10.1364/OE.20.021457

Kokhanovsky, A. A., Breon, F. M., Cacciari, A., Carboni, E., Diner, D., di Nicolantonio, W., et al. (2007). Aerosol remote sensing over land: A comparison of satellite retrievals using different algorithms and instruments. *Atmospheric Research*, *85*(3-4), 372–394. https://doi.org/10.1016/j.atmosres.2007.02.008

Lebsock, M. D., L'Ecuyer, T. S., & Stephens, G. L. (2007). Information content of near-infrared spaceborne multiangular polarization measurements for aerosol retrievals. *Journal of Geophysical Research*, *112*, D14206. https://doi.org/10.1029/2007JD008535

Levy, R. C., Remer, L. A., Mattoo, S., Vermote, E. F., & Kaufman, Y. J. (2007). Second-generation operational algorithm: Retrieval of aerosol properties over land from inversion of Moderate Resolution Imaging Spectroradiometer spectral reflectance. *Journal of Geophysical Research*, *112*, D13211. https://doi.org/10.1029/2006JD007811

Levy, R. C., Remer, L. A., Kleidman, R. G., Mattoo, S., Ichoku, C., Kahn, R., & Eck, T. F. (2010). Global evaluation of the Collection 5 MODIS Dark-Target aerosol products over land. *Atmospheric Chemistry and Physics*, *10*(21), 10,399–10,420. https://doi.org/10.5194/acp-10-10399-2010

Li, Z., Goloub, P., Dubovik, O., Blarel, L., Zhang, W., Podvin, T., et al. (2009). Improvements for ground-based remote sensing of atmospheric aerosol properties by additional polarimetric measurements. *Journal of Quantitative Spectroscopy and Radiation*, *110*(17), 1954–1961. https://doi.org/10.1016/j.jqsrt.2009.04.009

Li, Z., Zhang, Y., Shao, J., Li, B., Hong, J., Liu, D., et al. (2016). Remote sensing of atmospheric particulate mass of dry PM2.5 near the ground: Method validation using ground-based measurements. *Remote Sensing of Environment*, *173*, 59–68. https://doi.org/10.1016/j.rse.2015.11.019

Li, Z. Q., Xu, H., Li, K. T., Li, D. H., Xie, Y. S., Li, L., et al. (2018). Comprehensive study of optical, physical, chemical and radiative properties of total columnar atmospheric aerosols over China: An overview of Sun-sky radiometer Observation NETwork (SONET) measurements. *Bulletin of the American Meteorological Society*, *99*(4). https://doi.org/10.1175/bams-d-17-0133.1

Litvinov, P., Hasekamp, O., & Cairns, B. (2011). Models for surface reflection of radiance and polarized radiance: Comparison with airborne multi-angle photopolarimetric measurements and implications for modeling top-of-atmosphere measurements. *Remote Sensing of Environment*, *115*(2), 781–792. https://doi.org/10.1016/j.rse.2010.11.005

Ma, Y., Li, Z., Li, Z., Xie, Y., Fu, Q., Li, D., et al. (2016). Validation of MODIS aerosol optical depth retrieval over mountains in Central China based on a Sun-sky radiometer site of SONET. *Remote Sensing*, *8*(12), 111. https://doi.org/10.3390/rs8020111

Maignan, F., Bréon, F.-M., Fédèle, E., & Bouvier, M. (2009). Polarized reflectances of natural surfaces: Spaceborne measurements and analytical modeling. *Remote Sensing of Environment*, *113*(12), 2642–2650. https://doi.org/10.1016/j.rse.2009.07.022

Marbach, T., Riedi, J., Lacan, A., & Schlüssel, P. (2015). The 3MI mission: Multi-viewing-channel-polarisation imager of the EUMETSAT polar system: Second generation (EPS-SG) dedicated to aerosol and cloud monitoring, paper presented at SPIE Optical Engineering + Applications. *Proceedings of SPIE*, *9613*, 961310-1-8. https://doi.org/10.1117/12.2186978

Martonchik, J. V., Kahn, R. A., & Diner, D. J. (2009). Retrieval of aerosol properties over land using MISR observations. In A. A. Kokhanovsky & G. de Leeuw (Eds.), *Satellite aerosol remote sensing over land* (pp. 267–292). Chichester, UK: Springer. https://doi.org/10.1007/978-3-540-69397-0_9

Martynenko, D., Holzer-Popp, T., Elbern, H., & Schroedter-Homscheidt, M. (2010). Understanding the aerosol information content in multi-spectral reflectance measurements using a synergetic retrieval algorithm. *Atmospheric Measurement Techniques*, *3*(6), 1589–1598. https://doi.org/10.5194/amt-3-1589-2010

Mishchenko, M. I., & Travis, L. D. (1997). Satellite retrieval of aerosol properties over the ocean using polarization as well as intensity of reflected sunlight. *Journal of Geophysical Research*, *102*(D14), 16,989–17,013. https://doi.org/10.1029/96JD02425

Mishchenko, M. I., & Travis, L. D. (1998). Capabilities and limitations of a current FORTRAN implementation of the T-matrix method for randomly oriented, rotationally symmetric scatterers. *Journal of Quantitative Spectroscopy and Radiation*, *60*(3), 309–324. https://doi.org/10.1016/S0022-4073(98)00008-9

Mishchenko, M. I., Cairns, B., Hansen, J. E., Travis, L. D., Burg, R., Kaufman, Y. J., et al. (2004). Monitoring of aerosol forcing of climate from space: Analysis of measurement requirements. *Journal of Quantitative Spectroscopy and Radiation*, *88*(1-3), 149–161. https://doi.org/10.1016/j.jqsrt.2004.03.030

Mishchenko, M. I., Cairns, B., Hansen, J. E., Travis, L. D., Kopp, G., Schueler, C. F., et al. (2007). Accurate monitoring of terrestrial aerosols and total solar irradiance: Introducing the Glory Mission. *Bulletin of the American Meteorological Society*, *88*(5), 677–691. https://doi.org/10.1175/bams-88-5-677

Patterson, E. M., Gillette, D. A., & Stockton, B. H. (1977). Complex index of refraction between 300 and 700 nm for Saharan aerosols. *Journal of Geophysical Research*, *82*(21), 3153–3160. https://doi.org/10.1029/JC082i021p03153

Peralta, R. J., Nardell, C., Cairns, B., Russell, E. E., Travis, L. D., Mishchenko, M. I., et al. (2007). Aerosol polarimetry sensor for the Glory Mission. *Proceedings of SPIE*, *6786*, 67,861–67,817. https://doi.org/10.1117/12.783307

Qie, L., Li, Z., Sun, X., Sun, B., Li, D., Liu, Z., et al. (2015). Improving remote sensing of aerosol optical depth over land by polarimetric measurements at 1640 nm: Airborne test in North China. *Remote Sensing*, *7*(12), 6240–6256. https://doi.org/10.3390/rs70506240

Ramachandran, S. (2007). Aerosol optical depth and fine mode fraction variations deduced from Moderate Resolution Imaging Spectroradiometer (MODIS) over four urban areas in India. *Journal of Geophysical Research*, *112*, D16207. https://doi.org/10.1029/2007JD008500

Rodgers, C. D. (2000). *Inverse methods for atmospheric sounding: Theory and practice*. Singapore: World Scientific. https://doi.org/10.1142/3171

Roujean, J.-L., Leroy, M., & Deschamps, P.-Y. (1992). A bidirectional reflectance model of the Earth's surface for the correction of remote sensing data. *Journal of Geophysical Research*, *97*(D18), 20455–20,468. https://doi.org/10.1029/92JD01411

Santer, R., Carrere, V., Dubuisson, P., & Roger, J. C. (1999). Atmospheric correction over land for MERIS. *International Journal of Remote Sensing*, *20*(9), 1819–1840. https://doi.org/10.1080/014311699212506

Sayer, A. M., Thomas, G. E., Grainger, R. G., Carboni, E., Poulsen, C., & Siddans, R. (2012). Use of MODIS-derived surface reflectance data in the ORAC-AATSR aerosol retrieval algorithm: Impact of differences between sensor spectral response functions. *Remote Sensing of Environment*, *116*, 177–188. https://doi.org/10.1016/j.rse.2011.02.029

Spurr, R. (2004). A new approach to the retrieval of surface properties from earthshine measurements. *Journal of Quantitative Spectroscopy and Radiation*, *83*(1), 15–46. https://doi.org/10.1016/S0022-4073(02)00283-2

Spurr, R. (2006). VLIDORT: A linearized pseudo-spherical vector discrete ordinate radiative transfer code for forward model and retrieval studies in multilayer multiple scattering media. *Journal of Quantitative Spectroscopy and Radiation*, *102*(2), 316–342. https://doi.org/10.1016/j.jqsrt.2006.05.005

Spurr, R. (2012). *User's guide VLIDORT version 2.6*. Cambridge, MD: RT solutions, Inc.

Spurr, R., Wang, J., Zeng, J., & Mishchenko, M. I. (2012). Linearized T-matrix and Mie scattering computations. *Journal of Quantitative Spectroscopy and Radiation*, *113*(6), 425–439. https://doi.org/10.1016/j.jqsrt.2011.11.014

Strahler, A. H., Lucht, W., Schaaf, C. B., Tsang, T., Gao, F., Li, X., et al. (1997). MODIS BRDF/albedo product: Algorithm theoretical basis document version 5.0.

Sun, L., He, G., Wang, Y., & Fang, L. (2009). An active set quasi-Newton method with projected search for bound constrained minimization. *Computers & Mathematcs with Applications*, *58*(1), 161–170. https://doi.org/10.1016/j.camwa.2009.03.085

Sun, L., He, G., Wang, Y., & Changyin, Z. (2011). An accurate active set newton algorithm for large scale bound constrained optimization. *Applications of Mathematics*, *56*(3), 297–314. https://doi.org/10.1007/s10492-011-0018-z

Tanré, D., Herman, M., & Kaufman, Y. J. (1996). Information on aerosol size distribution contained in solar reflected spectral radiances. *Journal of Geophysical Research*, *101*(D14), 19,043–19,060. https://doi.org/10.1029/96JD00333

Tanré, D., Bréon, F. M., Deuzé, J. L., Dubovik, O., Ducos, F., François, P., et al. (2011). Remote sensing of aerosols by using polarized, directional and spectral measurements within the A-Train: The PARASOL mission. *Atmospheric Measurement Techniques*, *4*(7), 1383–1395. https://doi.org/10.5194/amt-4-1383-2011

Thomas, G. E., Carboni, E., Sayer, A. M., Poulsen, C. A., Siddans, R., & Grainger, R. G. (2009). Oxford-RAL Aerosol and Cloud (ORAC): Aerosol retrievals from satellite radiometers. In A. A. Kokhanovsky & G. de Leeuw (Eds.), *Satellite aerosol remote sensing over land* (pp. 193–225). Chichester, UK: Springer. https://doi.org/10.1007/978-3-540-69397-0_7

Torres, O., Tanskanen, A., Veihelmann, B., Ahn, C., Braak, R., Bhartia, P. K., et al. (2007). Aerosols and surface UV products from Ozone Monitoring Instrument observations: An overview. *Journal of Geophysical Research*, *112*, D24S47. https://doi.org/10.1029/2007JD008809

Veihelmann, B., Levelt, P. F., Stammes, P., & Veefkind, J. P. (2007). Simulation study of the aerosol information content in OMI spectral reflectance measurements. *Atmospheric Chemistry and Physics*, *7*(12), 3115–3127. https://doi.org/10.5194/acp-7-3115-2007

von Hoyningen-Huene, W., Freitag, M., & Burrows, J. B. (2003). Retrieval of aerosol optical thickness over land surfaces from top-of-atmosphere radiance. *Journal of Geophysical Research*, *108*(D9), 4260. https://doi.org/10.1029/2001JD002018

Wagner, R., Ajtai, T., Kandler, K., Lieke, K., Linke, C., Müller, T., et al. (2012). Complex refractive indices of Saharan dust samples at visible and near UV wavelengths: A laboratory study. *Atmospheric Chemistry and Physics*, *12*(5), 2491–2512. https://doi.org/10.5194/acp-12-2491-2012

Wang, J., Christopher, S. A., Brechtel, F., Kim, J., Schmid, B., Redemann, J., et al. (2003). Geostationary satellite retrievals of aerosol optical thickness during ACE-Asia. *Journal of Geophysical Research*, *108*(D23), 8657. https://doi.org/10.1029/2003JD003580

Wang, J., Christopher, S. A., Reid, J. S., Maring, H., Savoie, D., Holben, B. N., et al. (2003). GOES 8 retrieval of dust aerosol optical thickness over the Atlantic Ocean during PRIDE. *Journal of Geophysical Research*, *108*(D19), 8595. https://doi.org/10.1029/2002JD002494

Wang, J., Xu, X., Spurr, R., Wang, Y., & Drury, E. (2010). Improved algorithm for MODIS satellite retrievals of aerosol optical thickness over land in dusty atmosphere: Implications for air quality monitoring in China. *Remote Sensing of Environment*, *114*(11), 2575–2583. https://doi.org/10.1016/j.rse.2010.05.034

Wang, H., Sun, X., Sun, B., Liang, T., Li, C., & Hong, J. (2014). Retrieval of aerosol optical properties over a vegetation surface using multi-angular, multi-spectral, and polarized data. *Advances in Atmospheric Sciences*, *31*(4), 879–887. https://doi.org/10.1007/s00376-013-3100-5

Wang, J., Xu, X., Ding, S., Zeng, J., Spurr, R., Liu, X., et al. (2014). A numerical testbed for remote sensing of aerosols, and its demonstration for evaluating retrieval synergy from a geostationary satellite constellation of GEO-CAPE and GOES-R. *Journal of Quantitative Spectroscopy and Radiation*, *146*, 510–528. https://doi.org/10.1016/j.jqsrt.2014.03.020

Wang, H., Sun, X., Hou, W., Chen, C., & Hong, J. (2015). Retrieval of aerosol optical thickness over land from airborne polarized measurements in Tianjin and Tangshan. *Proceedings of SPIE*, *9521*, 952119. https://doi.org/10.1117/12.2177561

Wang, J., Aegerter, C., Xu, X., & Szykman, J. J. (2016). Potential application of VIIRS day/night band for monitoring nighttime surface PM2.5 air quality from space. *Atmospheric Environment*, *124*, 55–63. https://doi.org/10.1016/j.atmosenv.2015.11.013

Wang, Y., Wang, J., Levy, R. C., Xu, X., & Reid, J. S. (2017). MODIS retrieval of aerosol optical depth over turbid coastal water. *Remote Sensing*, *9*(6), 595. https://doi.org/10.3390/rs9060595

Wanner, W., Li, X., & Strahler, A. H. (1995). On the derivation of kernels for kernel-driven models of bidirectional reflectance. *Journal of Geophysical Research*, *100*(D10), 21,077–21,089. https://doi.org/10.1029/95JD02371

Waquet, F., Léon, J.-F., Goloub, P., Pelon, J., Tanré, D., & Deuzé, J.-L. (2005). Maritime and dust aerosol retrieval from polarized and multispectral active and passive sensors. *Journal of Geophysical Research*, *110*, D10S10. https://doi.org/10.1029/2004JD004839

Waquet, F., Goloub, P., Deuzé, J. L., Léon, J. F., Auriol, F., Verwaerde, C., et al. (2007). Aerosol retrieval over land using a multiband polarimeter and comparison with path radiance method. *Journal of Geophysical Research*, *112*, D111214. https://doi.org/10.1029/2006JD008029

Waquet, F., Cairns, B., Knobelspiesse, K., Chowdhary, J., Travis, L. D., Schmid, B., & Mishchenko, M. I. (2009). Polarimetric remote sensing of aerosols over land. *Journal of Geophysical Research*, *114*, D01206. https://doi.org/10.1029/2008JD010619

Waquet, F., Léon, J.-F., Cairns, B., Goloub, P., Deuzé, J.-L., & Auriol, F. (2009). Analysis of the spectral and angular response of the vegetated surface polarization for the purpose of aerosol remote sensing over land. *Applied Aptics*, *48*(6), 1228–1236. https://doi.org/10.1364/AO.48.001228

Xie, D., Cheng, T., Zhang, W., Yu, J., Li, X., & Gong, H. (2013). Aerosol type over east Asian retrieval using total and polarized remote sensing. *Journal of Quantitative Spectroscopy and Radiation*, *129*, 15–30. https://doi.org/10.1016/j.jqsrt.2013.05.028

Xu, X., & Wang, J. (2015). Retrieval of aerosol microphysical properties from AERONET photopolarimetric measurements: 1. Information content analysis. *Journal of Geophysical Research: Atmospheres*, *120*, 7059–7078. https://doi.org/10.1002/2015JD023108

Xu, X., Wang, J., Henze, D. K., Qu, W., & Kopacz, M. (2013). Constraints on aerosol sources using GEOS-Chem adjoint and MODIS radiances, and evaluation with multisensor (OMI, MISR) data. *Journal of Geophysical Research: Atmospheres*, *118*, 6396–6413. https://doi.org/10.1002/jgrd.50515

Xu, X., Wang, J., Zeng, J., Spurr, R., Liu, X., Dubovik, O., et al. (2015). Retrieval of aerosol microphysical properties from AERONET photopolarimetric measurements: 2. A new research algorithm and case demonstration. *Journal of Geophysical Research: Atmospheres*, *120*, 7079–7098. https://doi.org/10.1002/2015JD023113

Xu, F., van Harten, G., Diner, D. J., Kalashnikova, O. V., Seidel, F. C., Bruegge, C. J., & Dubovik, O. (2017). Coupled retrieval of aerosol properties and land surface reflection using the Airborne Multiangle SpectroPolarimetric Imager. *Journal of Geophysical Research: Atmospheres*, *122*, 7004–7026. https://doi.org/10.1002/2017JD026776

Xu, X., Wang, J., Wang, Y., Henze, D. K., Zhang, L., Grell, G. A., et al. (2017). Sense size-dependent dust loading and emission from space using reflected solar and infrared spectral measurements: An observation system simulation experiment. *Journal of Geophysical Research: Atmospheres*, *122*, 8233–8254. https://doi.org/10.1002/2017JD026677

Xu, X., Wang, J., Wang, Y., Zeng, J., Torres, O., Yang, Y., et al. (2017). Passive remote sensing of altitude and optical depth of dust plumes using the oxygen A and B bands: First results from EPIC/DSCOVR at Lagrange-1 point. *Geophysical Research Letters*, *44*, 7544–7554. https://doi.org/10.1002/2017GL073939

Yu, H., Chin, M., Remer, L. A., Kleidman, R. G., Bellouin, N., Bian, H., & Diehl, T. (2009). Variability of marine aerosol fine-mode fraction and estimates of anthropogenic aerosol component over cloud-free oceans from the Moderate Resolution Imaging Spectroradiometer (MODIS). *Journal of Geophysical Research*, *114*, D10206. https://doi.org/10.1029/2008JD010648

Yu, J., Li, M., Wang, Y., & He, G. (2014). A decomposition method for large-scale box constrained optimization. *Applied Mathematics and Computation*, *231*, 9–15. https://doi.org/10.1016/j.amc.2013.12.169

Zhang, Y., Li, Z., Qie, L., Zhang, Y., Liu, Z., Chen, X., et al. (2016). Retrieval of aerosol fine-mode fraction from intensity and polarization measurements by PARASOL over East Asia. *Remote Sensing*, *8*(12), 417. https://doi.org/10.3390/rs8050417

Zhu, C., Byrd, R. H., Lu, P., & Nocedal, J. (1994). *L-BFGS-B – Fortran subroutines for large-scale bound constrained optimization, Edited*. Evanston: Northwestern University.

Zubko, V., Kaufman, Y. J., Burg, R. I., & Martins, J. V. (2007). Principal component analysis of remote sensing of aerosols over oceans. *IEEE Transactions on Geoscience and Remote*, *45*(3), 730–745. https://doi.org/10.1109/TGRS.2006.888138